A two-way coupling method for simulating wave-induced breakup of ice floes based on SPH

Ningbo Zhang[a], Qingwei Ma[a], Xing Zheng[b,*], Shiqiang Yan[a]

[a] School of Mathematics, Computer Science and Engineering, City University of London, London EC1V 0HB, UK,
[b] College of Shipbuilding Engineering, Harbin Engineering University, Harbin 150001, China

***** Correspondence: zhengxing@hrbeu.edu.cn

Abstract

In this paper, a new numerical method for simulating the breakup of ice floes in water waves will be presented. The method is based on Smoothed Particle Hydrodynamics (SPH) but several new numerical techniques are developed to address the challenges associated with wave-ice interaction including breakup. One of them is the new interaction model for fluid-ice interaction, which is not only suitable for small density ratio but also for large density ratio. This model may also be employed by other methods for dealing with general fluid-structure integration. In addition, a technique for modelling the separation of broken ice pieces is developed. Apart from these, a treatment is proposed to rectify the problem caused by unequal time steps in simulating ice and fluid, which is necessary for achieving higher computational efficiency. The numerical method is validated by comparing the numerical results with the experimental data available in literature, which shows that the agreement between them is satisfactory. On this basis, the breakup of ice floes induced by solitary waves and focused waves are studied. To the best of knowledge of the authors, it is the first method which can simulate the ice breaking in waves by two-way coupling approach. The results for ice breaking in solitary and focused waves have not been found so far in previous publications available in literature.

Keywords: SPH; wave-induced breakup; ice floe; fluid-ice interaction; coupling method

Nomenclature

v	velocity	l	fracture length
p	pressure	Y_m	maximum heave displacement
g	gravitational acceleration	A_f	wave amplitude
q	speed of sound	G	shear modulus
$\boldsymbol{n}$	unit normal vector		
a	acceleration	*Greek symbols*	
s	deviatoric shear stress	ρ	density
c	ice cohesion	Γ	viscous shear stress
m	mass of particle	μ	kinematic viscosity
N (M)	particle numbers	σ	stress
W	kernel function	Π	artificial viscous term
h	kernel smoothing length	$\dot{\varepsilon}$	strain rate
ΔV	volume of particle	υ	Poisson's ratio
r	position	ϕ , φ	friction and dilatancy angle
R	artificial stress	σ_f	flexural strength
dx	initial particle spacing	$\bar{\varepsilon}_p$	accumulated plastic strain
Δt	time step	$\dot{\varepsilon}_{ev}$	volumetric strain rate
K	bulk modulus	$\dot{e}^{\alpha\beta}$	deviatoric shear strain rate
$F^{\alpha}_{I\ fluid-ice}$	force on an ice particle I from its neighbouring fluid particles	$\dot{\lambda}$	plastic multiplier rate
$F^{\alpha}_{f\ ice-fluid}$	force on the fluid particle f from its neighbouring ice particles	*Subscripts and subscripts*	
d	distance from the boundary to particle	t	time
dl	length between particles	α , β	dimensional indexs
E	Young's modulus	x , y	Cartesian coordinates
D	water depth	$f(l)$	physical quantity of fluid
L_i	length of ice floe	i, $I(j)$	physical quantity of ice
th_i	thickness of ice floe	dum	dummy particle
H, T	wave height and period	b	physical quantity of boundary

1. Introduction

Wave-ice interaction exists in the marginal ice zone (MIZ) of ocean. During the interactions, ocean waves can cause the ice to break (Squire, 2007, 2011; Kohout et al., 2016; Steele, 1992; Herman, 2017). The broken ice pieces have different sizes. These with their horizontal sizes much larger than the wavelength are called as ice sheets while these have their horizontal sizes in the same order of the wavelength called as ice

floes. The broken ices can have significant effects on the performance of ships and structures operating in the MIZ. Therefore, there is great demanding on understand the mechanism of sea-ice breakup under wave impact. To do so, one may use either experimental or numerical methods. As indicated by its title, this paper will develop a numerical method and so the literature review below will focus on numerical studies.

Different numerical approaches have been adopted for studying the ice floes and ice sheets. To study ice-sheet interaction with waves, researchers treated the ice sheets as a think elastic and plastic plate. For example, Meylan et al. (2015) used the linear potential flow and plastic thin-plate theories to study the flexural motion of an ice plate induced by ocean waves; and Wang and Shen (2011) developed a continuum viscoelastic model, in which an approximate solution was presented for the linear wave interaction with a large ice sheet. To study ice floes, many researchers have considered them as a rigid block. Bai et al. (2017) used the potential flow model and the viscous flow method to investigate the kinematic response of rigid ice floes in waves. Yiew (2017) studied collision of two rigid ice floes floating in waves. Shen and Ackley (1991) also studied the collision of rigid ice floes in waves by approximating the wave field as a variable gravity field. Considering the ice floes as a rigid block may be suitable only for very small ice floes. Fewer researchers did treat the ice floes as deformable but nonbreaking bodies. Squire (1981) proposed a numerical model based on finite element techniques to compute the flexure of an arbitrarily shaped ice floe in ocean waves. Zhang et al. (2019) developed a two-dimensional model to study the deformation and stress of the ice floes.

In the above references, the breakup of ice floes under ocean waves are fully neglected. The other area of study which partially considered the ice break-up was on the ice floe size distribution. Dumont et al. (2011) proposed a numerical model incorporating a simple parameterization for ice floe breaking and a wave scattering model in a one-dimensional numerical framework to study the floe size distribution in MIZ. Williams et al. (2013 a,b) presented a wave-ice interaction model which includes wave attenuation due to the presence of ice cover and the breakup of ice by the waves. They used a probabilistic approach to obtain the breaking criterion. Montiel and Squire (2017) coupled a three-dimensional linear model of ocean wave with a parametrisation of flexural failure model for ice floe. They mainly focus on gaining a theoretical understanding of how floe size distribution evolves under repeated wave action. Based on a linear water wave theory and viscoelastic sea ice rheology, Mokus and Montiel (2021) proposed a two-dimensional numerical model for the wave-triggered sea ice breakup. Their model included the wave scattering and dissipation and a strain-based breakup parametrisation. They also focused on the ice floe size distribution. Zhang and Zhao (2021) presented an approximate method including a 2D ice breakup based on the stress break-up criterion and the MC stress break-up criterion for predicting the ice floe break-up under ocean wave forcing in the MIZ. Their model was also designed to

facilitate the prediction of the ice floe size. While these investigations provided a good prediction of the floe size distribution, the detailed physical processes of the wave-ice interaction, the ice deformation and breakup were not considered.

Toward revealing the physics of ice breakup caused by waves, several studies were carried out. Xu et al. (2012) proposed a discrete-element method (DEM), in which a given velocity field of waves was applied to each ice floe particle. The interaction between fluid and ice were not explicitly modelled in their work. He et al. (2022) presented a numerical model simulating the breakup of the ice under the regular incident wave based on the Computational Fluid Dynamics (CFD) -Discrete Element Method. Ren et al. (2021) used a peridynamics (PD) model to simulate the breakup of sea ice induced by regular waves with the drag forces estimated by an empirical model. The stress distribution and crack propagation path of the ice sheet were simulated. In the cited studies, one-way coupling approach was adopted. In other words, only the effect of waves on sea ice was considered, but the effects of the motion and breakup of ice floes on fluid dynamics were ignored.

In contrast, the present paper will consider both effects, i.e., adopting a two-way coupling approach. The method to be presented in this paper will be based on the Smoothed Particle Hydrodynamics (SPH) method. The recent extensive review on the SPH development may be found in Luo et al. (2021). A brief review will be only given below. SPH method has been widely applied to the ocean and coastal hydrodynamics (Morris et al., 1997; Shao and Lo, 2003; Shao, 2010; Khayyer et al., 2008; Zheng et al., 2014; Zhang et al., 2018; You et al., 2021). Because of its nature of Lagrangian formulation (Jiménez et al., 2018; Ren and Park, 2023), SPH can simulate the large deformations and failure behaviors of solid materials effectively. A few examples are mentioned here. Libersky and Petschek (1991) and then by Randles and Libersky (1996) used the SPH for investigation of large deformation and corresponding response of a solid material. Bui et al. (2008) studied the large deformation and post-failure of soil. Wang et al. (2020) modelled the mixed-mode fracture using the SPH method and mixed-mode cohesive fracture law. Ganesh et al. (2022) presented the pseudo-spring-based Eulerian form of SPH to model mode-I fatigue crack propagation. Mu et al. (2023) proposed an improved SPH method to simulate the failure process of rock with pre-existing cracks under compression loads. The SPH method has also received considerable attentions in the fluid-structure interaction (FSI) problems. Bui et al. (2007) introduced a SPH algorithm to simulate the interactions between water and soil. Joshi et al. (2019) developed an axisymmetric SPH FSI solver to simulate the collapse of a single cavitation bubble close to an elastic-plastic material. Antoci et al. (2007) proposed a SPH-based FSI solver to study the complex hydro-elastic problems.

Khayyer et al. (2021) carried out investigations on the fluid-elastic composite structures interactions by using a coupled incompressible SPH-Hamiltonian SPH solver. Khayyer et al. (2022) proposed the 3D SPH-based Lagrangian meshfree hydroelastic solver for reproduction of incompressible fluid flows interacting with anisotropic/isotropic composite elastic structures. Ren et al. (2023) applied a SPH model to investigate the sloshing flow interaction with an elastic baffle.

SPH method has also been applied to simulating ice dynamics. Gutfraind and Savage (1997) and Oger and Savage (1999) applied a rheology based on the Mohr–Coulomb yield criterion in the framework of SPH to study broken-ice fields floating on the water surface and moving under the effect of wind forces without water waves. Shen et al. (2000) presented a two-dimensional numerical model for dynamic transport and jamming of surface ice in rivers, in which ice dynamics is simulated by the SPH method. The moving ice on water surface is considered as a continuum and non-breaking. Ji et al. (2005) presented a viscoelastic-plastic (VEP) constitutive model for sea ice dynamics, where SPH method was used in the numerical simulations for ice motion under wind and current drags in an idealized rectangular basin without water waves. Ji et al. (2007) developed a hybrid Lagrangian-Eulerian (HLE) method for studying ice ridging under uniform current and wind field, in which ice is represented by SPH model with their own thicknesses and concentrations, again without considering water waves. Zhang et al. (2017) used the SPH method to simulate the bending and compression failure processes of ice block. Extending their work, Zhang et al. (2019) investigated the ship-ice interaction process. The effects of fluid on ice are not considered in both papers. They further extended their work in Zhang et al. (2019) to model the kinematic response and the flexural motion of ice floes in waves; however, the breakup of ice floe induced by waves was neglected.

In contrast with the current literature, this paper will develop a new method based on SPH. The new method will adopt two-way coupling approach, i.e, taking into account of wave effects on ice and ice effects on waves. To our best knowledge, this is first paper of this kind. To tackle the challenges associated with ice breakup and two-way coupling, new numerical techniques will be developed. These include a new model for dealing with the interaction between fluid and ice and a new separation model for breakup of ice. Apart from these, an unequal time-step scheme for simulating ice and fluid is adopted and the problem caused by the unequal time-step scheme is rectified by an effective treatment. The rest contents of the paper are organized as follows: Firstly, the governing equations including constitutive model for ice are introduced briefly. Then, some numerical formulations of SPH method are given in Section 3. After that, the details of new numerical techniques are described in Section 4. Following this, the convergent tests and validation on the proposed method will be carried out before applying the new method to study various cases for ice breaking in solitary and focusing

waves in Section 5.

2. Governing equations

2.1. Equations of Fluid

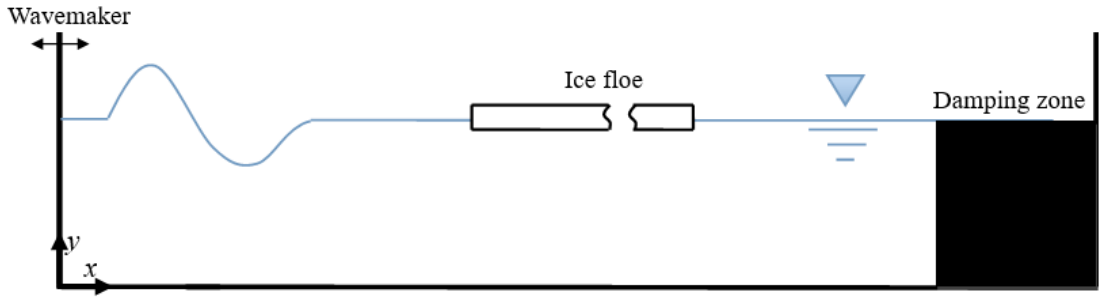

Fig. 1. Sketch of wave-induced breakup of ice floe

In this paper, the fluid (Fig. 1) is assumed to be weakly-compressible and the flow of fluid is governed by the mass and momentum conservation equations:

$$\frac{D\rho_f}{Dt} = -\rho_f \frac{\partial v_f{}^{\alpha}}{\partial x^{\alpha}} \tag{1}$$

$$\frac{Dv_f{}^{\alpha}}{Dt} = -\frac{1}{\rho}\frac{\partial p_f}{\partial x^{\alpha}} + g^{\alpha} + \Gamma_f{}^{\alpha} \tag{2}$$

where α indicates the Cartesian components in x or y directions; v, ρ and p with subscript f is the velocity, the density, the pressure of a fluid particle *f; g* is the gravitational acceleration; $\Gamma_f = \mu\nabla^2 v_f$ is viscous shear stress of fluid with μ being the kinematic viscosity; D/Dt is the time derivative operator following particle motions.

For a weakly compressible fluid, the following equation of state (EOS) is used, which defines the relation between pressure and density:

$$p_f = B\left[\left(\frac{\rho_f}{\rho_{f0}}\right)^{\gamma} - 1\right] \tag{3}$$

where $\gamma = 7$ and $B = \frac{q_f^2 \rho_{f0}}{\gamma}$, ρ_{f0} is reference density, q_f is the sound speed for fluid.

The above equations have been used widely in the SPH community, see for example, Bouscasse et al. (2013) and Ren et al. (2015).

On solid boundaries of the fluid phase, the following conditions (Ma and Zhou, 2009) should be imposed

$$\boldsymbol{v}_f \cdot \boldsymbol{n} = \boldsymbol{v}_b \cdot \boldsymbol{n} \tag{4}$$

$$\boldsymbol{n} \cdot \nabla p_f = \rho_f \left(\boldsymbol{n} \cdot \boldsymbol{g} - \boldsymbol{n} \cdot \boldsymbol{a}_b\right) \tag{5}$$

where $\boldsymbol{n}$ is the unit normal vector of the solid boundaries; $\boldsymbol{v}_b$ and $\boldsymbol{a}_b$ are the velocity and

acceleration of the solid boundaries, respectively. The boundary conditions on the interface between fluid and ice will be discussed later.

2.2. Equations and Constitutive Model of Ice

2.2.1 Equations of ice

The mass conservation equation for ice (Fig. 1) is the same as Eq. (1) and just needs to make the changes of $\rho_f \to \rho_I$ and $\boldsymbol{v}_f \to \boldsymbol{v}_I$. The momentum equation for ice is written as:

$$\frac{Dv_I^{\ \alpha}}{Dt} = \frac{1}{\rho_I}\frac{\partial \sigma_I^{\ \alpha\beta}}{\partial x^\beta} + g^\alpha \tag{6}$$

where v_I is the velocity of ice particle *I* and ρ_I is its density; $\sigma_I^{\ \alpha\beta}$ is its stress tensor.

The stress tensor can be divided into two parts: pressure p_I and deviatoric shear stress $\boldsymbol{s}_I$. Similar to Zhang et al. (2017), the pressure p_I is defined by $p_I = -\sigma_I^{\ \gamma\gamma}/3$ and the stress tensor may be expressed as:

$$\sigma_I^{\ \alpha\beta} = -p_I\delta^{\alpha\beta} + s_I^{\ \alpha\beta} \tag{7}$$

in which $\delta^{\alpha\beta}$ is the Kronecker delta and satisfy the following conditions: $\delta^{\alpha\beta} = 1$ for $\alpha = \beta$ or $\delta^{\alpha\beta} = 0$ for $\alpha \neq \beta$.

2.2.2 Constitutive Model of ice

The constitutive model depends on the failure mode. Ice is a strain-rate-dependent material. At low strain rate, ice has a ductile behaviour. It fails mainly in creep and micro-cracking mode and can be treated as a viscous elastic material (Jordaan, 2001). At high strain rates (>0.001 1/s), ice exhibits the typical brittle failure mode (Schulson, 2001); as a result, the visco-plastic effect is considered weak, and the elastoplastic constitutive model can be employed (Shi et al., 2017). Based on our previous study, the strain rate is high during failure process of ice. Thus, the same elastoplastic constitutive model of ice as that of Zhang et al. (2017) will be employed here. In addition, according to Sanderson (1988), old ice is conventionally treated as an isotropic material, and first-year ice possesses a typical orthotropic property in its mechanical behaviours. The relatively simple isotropic ice model is used in this paper as our focus here is on a numerical method. More complex ice model considering the anisotropy, the temperature dependence and visco-elastic-plastic behaviours of the ice will be explored in the future study.

For completeness, the details of the ice model are given in Appendix A. This model was developed on the basis of Bui et al. (2008) and Deb and Pramanik (2013) for simulating the failure process of ice. It combines the elastoplastic constitutive model

with the Drucker-Prager yield criterion and cohesion softening. In the model, the behaviour of ice is determined by the yield function $F(\sigma^{\alpha\beta}, c)$ as defined in the Appendix A. When $F(\sigma^{\alpha\beta}, c) < 0$, ice is in elastic stage and the stress and strain satisfies the generalized Hooke's law. When $F(\sigma^{\alpha\beta}, c) > 0$, ice is in the plastic state and the stress-strain follows a nonlinear relationship. During this stage, the stress needs to be corrected to keep $F(\sigma^{\alpha\beta}, c) \approx 0$. In addition, the cohesion of ice is softened to model the effect of fracturing or cracking. The whole procedure is illustrated in Fig. 2. This model has been validated for the cases about three-point bending and four-point bending failures of the ice beam in our previous publications (Zhang et al. 2017 and Zhang et al., 2019)

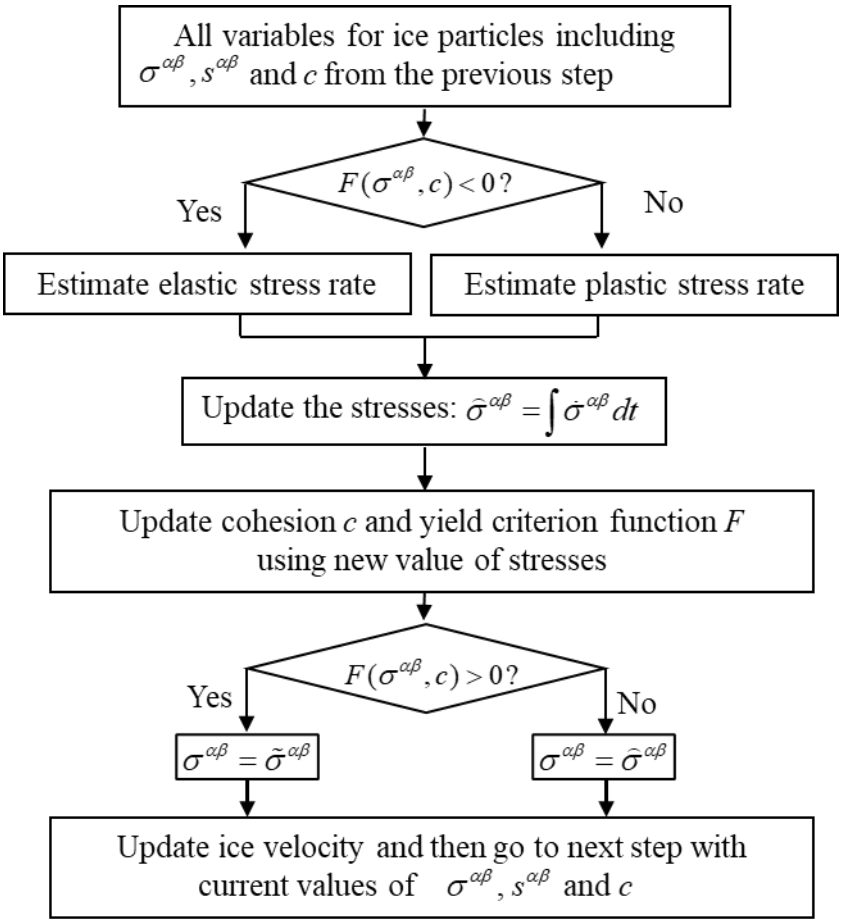

Fig. 2. Procedure of numerical implementation of the elastic–plastic ice model with the details given in Appendix A.

3. SPH formulations

In the SPH method, the quantities of a particle can be approximated by the direct summation of the relevant quantities of its neighbouring particles. For convenience of

explanation, we use subscripts f (l) and I (j) to indicate fluid and ice particles, respectively, in the following SPH equations.

The continuity equation for an ice particle can be approximated as follows:

$$\frac{D\rho_I}{Dt} = \rho_I \sum_{j=1}^{N_I} \frac{m_j}{\rho_j} \left(v_I^\alpha - v_j^\alpha \right) \frac{\partial W_{Ij}}{\partial x_I^\alpha} \tag{8}$$

where m_j is the mass of Particle j, N_I is the number of ice neighbour particles; W is a kernel function, chosen as the quintic kernel proposed by Wendland (1995).

The continuity equation for fluid will be approximated by δ-SPH scheme (Antuono et al., 2010) with a proper artificial diffusive term, i.e.:

$$\frac{D\rho_f}{Dt} = \sum_{l=1}^{N_f} \Delta V_l \left[\rho_f \left(v_f^\alpha - v_l^\alpha \right) + \delta h c_0 \psi_{fl} \right] \frac{\partial W_{fl}}{\partial x_f^\alpha} \tag{9}$$

where h is the kernel smoothing length, ΔV_l is the volume of particle l and N_f is the number of fluid neighbour particles, $\psi_{fl} = 2\left(\rho_l - \rho_f\right) \frac{\boldsymbol{r}_{fl}}{\left|\boldsymbol{r}_{fl}\right|^2} - \left[\langle \nabla \rho \rangle_f^L + \langle \nabla \rho \rangle_l^L \right]$,

$\langle \nabla \rho \rangle_f^L = \sum_l \left(\rho_l - \rho_f\right) \boldsymbol{L}_f \nabla_f W_{fl} \Delta V_l$ and $\boldsymbol{L}_f = \left[\sum_l \left(r_l - r_f \right) \otimes \nabla_f W_{fl} \Delta V_l \right]^{-1}$, in which $\boldsymbol{r}$ is the position vector and $\boldsymbol{r}_{fl} = \boldsymbol{r}_l - \boldsymbol{r}_f$. The coefficient δ controls the order of magnitude of the diffusive term and is set to be 0.01 in this paper. More details about the δ-SPH scheme can be found in Antuono et al. (2010). Summation is performed with superscripts α in Eq. (8) and (9).

The SPH approximation of the momentum equation for fluid can be written as:

$$\frac{dv_f^\alpha}{dt} = \sum_{l=1}^{N_f} m_l \left(-\frac{p_f + p_l}{\rho_f \rho_l} - \Pi_{fl} \right) \frac{\partial W_{fl}}{\partial x_f^\alpha} + g^\alpha \tag{10}$$

Note that the viscous shear stress in Eq. (2) contains second derivatives. In the corresponding SPH form (i.e., Eq. (10)), this term is replaced by an artificial viscous term Π_{fl}, as proposed by Monaghan and Gingold (1983).

The SPH approximation of the momentum equation for ice is similar but with the use of the artificial stress proposed by Monaghan (2000) and Gray et al. (2001). The main purpose of the artificial stress is to prevent the particle from clumping with neighbouring particles and to eliminate numerical instability (Swegle et al., 1995). The discretized form of the momentum equation for the ice particles is given by

$$\frac{dv_I^\alpha}{dt} = \sum_{j=1}^{N_I} m_j \left(\frac{\sigma_I^{\alpha\beta}}{\rho_I^2} + \frac{\sigma_j^{\alpha\beta}}{\rho_j^2} - \Pi_{Ij} \cdot \delta^{\alpha\beta} + f_{Ij}^n \left(R_I^{\alpha\beta} + R_j^{\alpha\beta} \right) \right) \frac{\partial W_{Ij}}{\partial x_I^\beta} + g^\alpha \tag{11}$$

where $R_I^{\alpha\beta}$ and $R_j^{\alpha\beta}$ is artificial stress tensor of particles I and j, respectively; and f_{Ij}

is defined as $f_{Ij}=W_{Ij}/W(dx,h)$ with dx being the initial particle spacing. Summation is performed with β in Eq. (11). More details about the artificial stress can be found in Zhang et al (2017) and Gray et al. (2001). It should be noted that the artificial viscosity and artificial repulsive stress terms in Eq (11) may bring unexpected effect on ice fracture behaviors if they are properly imposed. Therefore, it is critical to select appropriate values of relevant coefficients. Some numerical tests of the bending and compression failure progress of ice in Zhang et al. (2017) and Zhang (2019) has been carried out to select their values, which can lead to the satisfactory results for simulating the fracture behaviors of ice.

In addition, the movements of ice particles are estimated by using the XSPH method (Monaghan 1992),

$$\frac{Dx_I^\alpha}{Dt}=v_I^\alpha+\bar{\varepsilon}\sum_{j=1}^{N}\frac{m_j}{\rho_j}\left(v_j^\alpha-v_I^\alpha\right)W_{Ij},\quad \bar{\varepsilon}\in[0,1] \tag{12}$$

where $\bar{\varepsilon}$ is taken as 0.1 for the structure particle based on the suggestion of Antoci et al. (2007). The movement of fluid particles is estimated in the same way.

As seen in Appendix A, one needs to estimate the strain rate of ice for estimating the stresses. We use the Simplified Finite Difference Interpolation (SFDI) method (Ma, 2008) to do so. The SFDI formulas of the strain rate tensor in 2D cases can be given as:

$$\dot{\varepsilon}_I^{\alpha\beta}=\frac{1}{2}\left(\sum_{j=1,j\neq I}^{N_I}\frac{n_{I,\alpha}B_{ij,\beta}-n_{I,xy}B_{Ij,\alpha}}{n_{I,x}n_{I,y}-n_{I,xy}^2}\left(v_j^\alpha-v_I^\alpha\right)+\sum_{j=1,j\neq I}^{N_I}\frac{n_{I,\beta}B_{Ij,\alpha}-n_{I,xy}B_{Ij,\beta}}{n_{I,x}n_{I,y}-n_{I,xy}^2}\left(v_j^\beta-v_I^\beta\right)\right) \tag{13}$$

where $n_{I,m}=\sum_{j=1,j\neq I}^{N_I}\frac{(r_j^m-r_I^m)^2}{\left|\boldsymbol{r}_j-\boldsymbol{r}_I\right|^2}W\left(\boldsymbol{r}_{Ij}\right)$, $n_{I,xy}=\sum_{j=1,j\neq I}^{N_I}\frac{(r_j^x-r_I^x)(r_j^y-r_I^y)}{\left|\boldsymbol{r}_j-\boldsymbol{r}_I\right|^2}W\left(\boldsymbol{r}_{Ij}\right)$,

$B_{Ij,m}=\frac{(r_j^m-r_I^m)}{\left|\boldsymbol{r}_j-\boldsymbol{r}_I\right|^2}W\left(\boldsymbol{r}_{Ij}\right)$

in which $\alpha=x,y$, $\beta=x,y$ and $m=x,y$, r_j^m is the component of the position vector in x or y direction. Similarly, the derivative of other variables can also be calculated by this method. The enhanced performance of the SFDI method in solid mechanics can be found in Zhang et.al (2017, 2019).

4. Wave–ice interaction model for the breakup of ice floe

The main original contribution of this paper lies in proposing a method for simulating the interaction between wave and ice floe with possible breakup of ice. The novel numerical techniques will be detailed in the following subsections.

4.1. Multiple time steps

Th ice material and water have very different material features. Their dynamics are controlled by different physics. In order to numerically model them correctly and efficiently, the time steps for them should be different. By numerical tests in this and

our previous publications, the time step for ice should be taken as

$$\Delta t_I \le 0.3\left(\frac{h_I}{q_I}\right) \tag{14}$$

where h_I is the smoothing length in ice solver, $q_I = \sqrt{\frac{K}{\rho_I}}$ is the sound speed for ice, K is the bulk modulus.

Following the study of Bouscasse et al (2013), the time step for fluid should be chosen as

$$\Delta t_f \le 0.25 \cdot \min\left(\sqrt{\frac{h_f}{a_{f\max}}}, \frac{h_f}{q_f + v_{f\max}}\right) \tag{15}$$

where h_f is the smoothing length in fluid solver, $a_{f\max}$ and $v_{f\max}$ are the maximum acceleration and maximum velocity of fluid, respectively with q_f being the artificial sound speed of fluid, set to be $q_f = 10u_{\max}$.

Based on Eqs. (14) and (15), the maximum time step for fluid can be much larger than that for ice. If the former would be taken as the latter, the overall computing efficiency would be low and the computational time would be unnecessarily long. In order to achieve relatively higher computational efficiency without affecting the accuracy, the different time steps for ice and fluid will be used. The marching procedure is illustrated in Fig. 3.

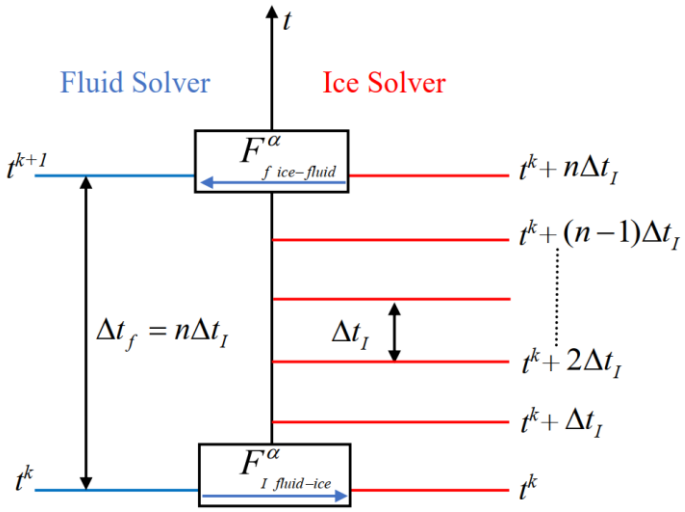

Fig. 3. The time marching procedure for modelling fluid and ice.

In this procedure, the time step Δt_I for modelling ice is determined by Eq. (14). The time step for modelling fluid is then given by $\Delta t_f = n\Delta t_I$, where n is an integer which

is selected properly to ensure that Eq. (15) is satisfied. For one time step of fluid modelling, such as from t^k to t^{k+1}, shown in **Fig. 3**, the fluid force at t^k acting on the ice remains the same until the end of $n\Delta t_I$ (more details will be discussed later). The solution of ice variables at $n\Delta t_I$ is transferred to fluids, and then the solution of fluid variables will be updated at t^{k+1}. After that, the procedure goes on to next time step. It is noted that the iteration between the fluid and ice solvers may be performed but it is not found unnecessary if the time steps are determined in the way described here.

4.2. Interaction model between ice and fluid particles

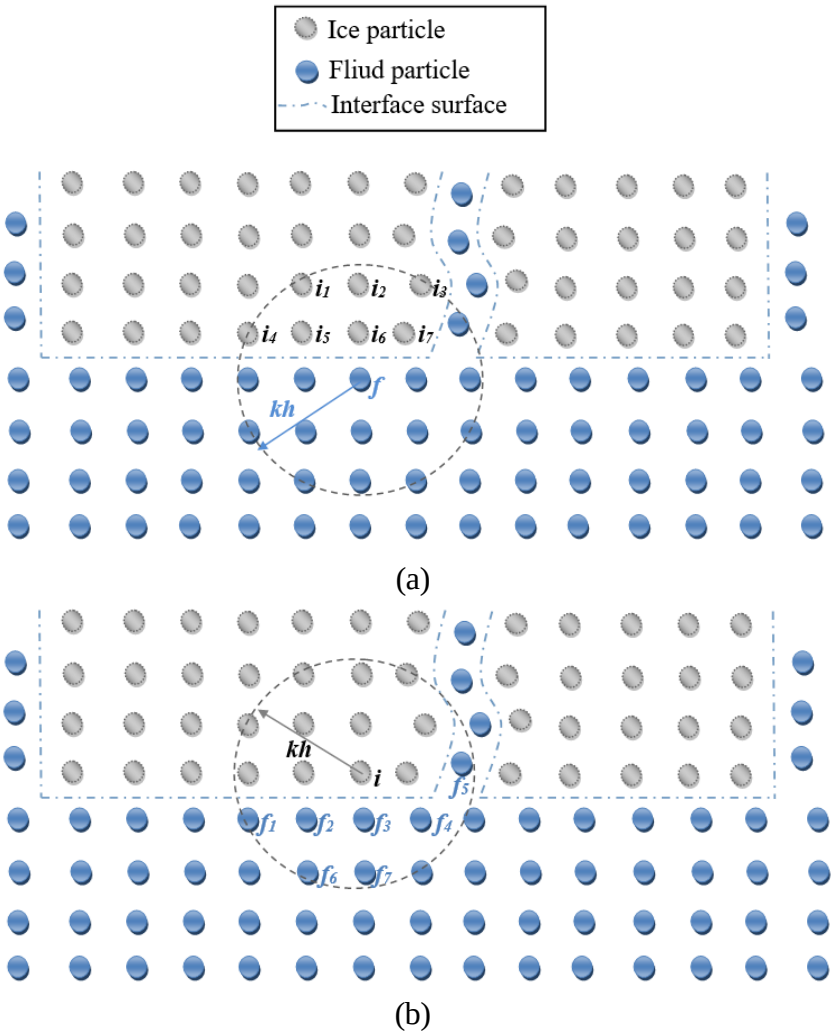

Fig. 4. A schematic diagram of fluid and ice particles at interface boundary.

In the procedure above, the exchange of information between fluid and ice should ensure that the kinematic and dynamic conditions on their interface are satisfied, i.e.,

$$\boldsymbol{v}_I = \boldsymbol{v}_f \tag{16}$$

$$\boldsymbol{\sigma}_I \cdot \boldsymbol{n}_{If} = -\boldsymbol{\sigma}_f \cdot \boldsymbol{n}_{If} \tag{17}$$

where $\boldsymbol{n}_{lf}$ is the normal vector of the interface. According to Antoci et al. (2007), the dynamic conditions in Eq. (17) cannot be directly fulfilled when the viscous shear stress for fluid phase is modelled as an artificial viscosity as given in Eq. (10).

Some studies on implementing the conditions in the SPH method have been conducted. An approximation of pressure gradient was used by Antoci et al. (2007). However, this method requires computation of the precise position of interface surface and its normal direction, which is difficult to achieve, especially in the cases with complex boundaries. In addition, the repulsive force method was proposed by Amini et al. (2011). In their approach, the repulsive force was not based on the clear mathematical–physical formulation. Due to this, the numerical complexity and instability can be caused by the uncertainty of the parameters. Adami et al. (2012) presented a generalized wall boundary method using dummy particles. Based on that method, He et al. (2017) developed a coupled WC-TL SPH formulation to solve hydro-elastic problems. In their work, an equivalent interfacial force from fluid is applied to the solid body. That method also needs identification of the interface particles and calculate their normal direction as in Antoci et al. (2007). Recently, Zhan et al. (2019) presented a unified approach for modeling fluid–deformable structure interfaces based on the approach proposed by Adami et al. (2012). These available schemes were developed to study the fluid–elastic structure interactions.

The focus of this paper is to model the wave-ice interaction with possible ice breakup, which was not considered previously. For this purpose, a new coupling scheme is proposed. In this scheme, similar to Adami et al. (2012) and Zhang et al. (2019), some ice particles in the support domain of the fluid particle near the interface, e.g. i_1, i_2....i_7 in Fig. 4(a), are considered as dummy particles for the corresponding fluid particle f. These dummy particles are regarded as the continuous fluid phase to fluid particles near the interface boundary. Consequently, the dummy particles make contributions to the continuity and momentum equations of its neighbour fluid particles. With these dummy particles, there will be extra terms in Eq. (9) and (10) for the fluid particles near the interface. They are respectively

$$\delta\rho_f = \rho_f \sum_{j=1}^{N_1} V_{j,dum}\left(v_f^\alpha - v_{j,dum}^\alpha\right)\frac{\partial W_{fj}}{\partial x_f^\alpha} \tag{18a}$$

$$F^\alpha_{f\ ice-fluid} = m_f \sum_{i=1}^{N_1} m_{i,dum}\left(-\frac{p_f + p_{i,dum}}{\rho_f \rho_{i,dum}} - \Pi_{fi,dum}\right)\frac{\partial W_{fi}}{\partial x_f^\alpha} \tag{18b}$$

where the variables with subscript *dum* represent these from dummy particles, and N_1 is the number of dummy particles in the neighbour of the fluid particle concerned. Eq. (18a) is to ensure that the density of fluid is correctly estimated. Each term on the right-hand side of Eq. (18b) represents a force from dummy particle on the fluid particles. Overall, Eq. (18b) approximates the force acting on fluid from ice.

Following Bouscasse et al. (2013) and Ren et al. (2015), the force on an ice particle

I from its neighbouring fluid particles (**Fig. 3b**) can be estimated by the following equation

$$F^{\alpha}_{I\ fluid-ice} = m_I \sum_{f \in fuid}^{N_2} m_f \left(-\frac{p_{i,dum} + p_f}{\rho_{i,dum}\rho_f} - \Pi_{if} \right) \frac{\partial W_{if}}{\partial x_i^{\alpha}} \tag{19}$$

where N_2 is the number of fluid particles in the neighbourhood of the ice particle. Since $\partial W_{fi} / \partial x_f^{\alpha} = -\partial W_{if} / \partial x_i^{\alpha}$, the interacting force between each pair of interacting particles *I* and *f* in Eq. (18b) and (19) can have the same modulus and opposite direction. Therefore, the momentum conservation for each pair can be ensured and the dynamic condition in Eq. (17) can be approximately met if the variables of the dummy particles are properly assigned. It is noted that the interaction forces between ice and fluid act exactly on the interface in theory. However, in the numerical practice, they are equivalently distributed into a small domain near the interface in the SPH formulation.

In this paper the density for ice near its boundary does not take into account of the effects of fluid particles. The sound speed for ice is much larger than the sound speed for fluid. Thus, the density fluctuation of the ice model can be much less than that of fluid particles. In addition, the motion of an ice particle (e.g., *I*) is much similar to that of its neighbouring particles (e.g., *j*) due to the cohesion and thus the corresponding velocity difference between the ice particles is small. As a result, the density fluctuation of ice particles calculated from Eq. (8) can be negligible, and so the density for an ice particle near the boundary can be estimated quite accurately even without considering the contributions from fluid particles. However, the story may be different for the ice particles near the fracturing surface. These ice particles tend to separate from their neighbouring particles, and so the velocity difference between an ice particle (e.g., *I*) and its neighbouring particle (e.g., *j*) can be significant, which may cause some density fluctuation. Nevertheless, the fluctuation may have relatively weak effects on the ice dynamics as the stresses becomes small for these particles as seen in Eq. (11). This issue may need to be further explored in future work. One may have noticed from the above discussions that the key issue is how to assign the position, volume, density, velocity and pressure to the dummy particles as well as how these dummy variables are adopted. For ease of implementation, the position, volume and density of the dummy particles are made equal to these of corresponding ice particles calculated by Eq. (8) and (11). The velocity and pressure of the dummy particles will be discussed separately in the next two subsections.

4.3. Velocity on dummy particles

The velocity of dummy particles plays three roles: involved in the momentum equation of dummy particles discussed in next section; used for estimating the gradient of velocity in evaluating the density of fluid in Eq. (18a); and for estimating the viscous terms in Eq. (18b) and (19). Different treatments may be applied according to Macia et

al. (2011) and Bouscasse et al. (2013). For the first and second roles, the velocity of dummy particles are assigned as the velocity of ice particles following the suggestion of Morris et al. (1997), which is acceptable based on our numerical tests.

For estimating the viscous term, the velocity $\boldsymbol{v}_{dum}$ of a dummy particle can be obtained by imposing the non-slip boundary condition,

$$\boldsymbol{v}_{dum} = \boldsymbol{v}_b + \frac{d_{bd}}{d_{bf}}\left(\boldsymbol{v}_b - \boldsymbol{v}_f\right) = \left(1 + \frac{d_{bd}}{d_{bf}}\right)\boldsymbol{v}_b - \frac{d_{bd}}{d_{bf}}\boldsymbol{v}_f \tag{20}$$

which is similar to that suggested by Takeda et al. (1994), where the $\boldsymbol{v}_b$ and $\boldsymbol{v}_f$ are the velocities of the boundary and fluid particles, respectively; and d_{bd} and d_{bf} are the distances from the boundary to the dummy and fluid particles, respectively. Since one dummy particle interact with several fluid particles, the resulting $\boldsymbol{v}_{dum}$ is estimated by summing all contributions of neighbour fluid particles f using the kernel function as weight

$$\boldsymbol{v}_{dum} = \frac{\sum_{f \in fluid}^{N_2}\left(1 + \frac{d_{bd}}{d_{bf}}\right)\boldsymbol{v}_b W_{df} - \sum_{f \in fluid}^{N_2}\frac{d_{bd}}{d_{bf}}\boldsymbol{v}_f W_{df}}{\sum_{f \in fluid}^{N_2} W_{df}} \tag{21}$$

where $\boldsymbol{v}_b$ is assumed to be the actual velocity of the ice particle nearest to the interface. The evaluation of $\frac{d_{bd}}{d_{bf}}$ will be discussed in next section.

4.4. Pressure on dummy particles

The pressure $p_{i,dum}$ of a dummy particle in Eq. (18b) and Eq. (19) needs to be estimated from the fluid particles. This pressure is only used for the computations of interactions between fluid and ice particles, different from the pressure of the ice floe. Nevertheless, the derivation of the pressure at the dummy particles should be based on the fact that the kinematic condition (Eq. 16) needs to be met and the pressure to be equal to the pressure on the interface when the point concerned approaches to the interface (Eq. 17). The derivation of this pressure $p_{i,dum}$ is given bellow.

Considering the pair of fluid particle f and the dummy particle i as shown in Fig. 5, the line connecting them intersects the interface at point s. For the fluid particle f near the interface surface, the momentum equation of fluid for determining the dummy pressure is assumed to be given

$$\frac{d\boldsymbol{v}_f}{dt} = -\frac{\nabla p_f}{\rho_f} + \boldsymbol{g} \tag{22}$$

In the equation, the viscosity is ignored. There are three reasons for doing so. One is to obtain a simpler and easy-implemented expression for $p_{i,dum}$. The second is that the interaction between wave and ice considered here is dominated by the wave dynamics

with the viscosity playing less important role. The third is that the results are acceptable as demonstrated in the sections below.

Similarly, the momentum equation for the dummy particles is written as

$$\frac{d\boldsymbol{v}_I}{dt} = -\frac{\nabla p_{idum}}{\rho_I} + \boldsymbol{g} \tag{23}$$

It is noted that the velocity and density of the dummy particle have been taken as the velocity and density of ice at the same position as discussed in the previous section.

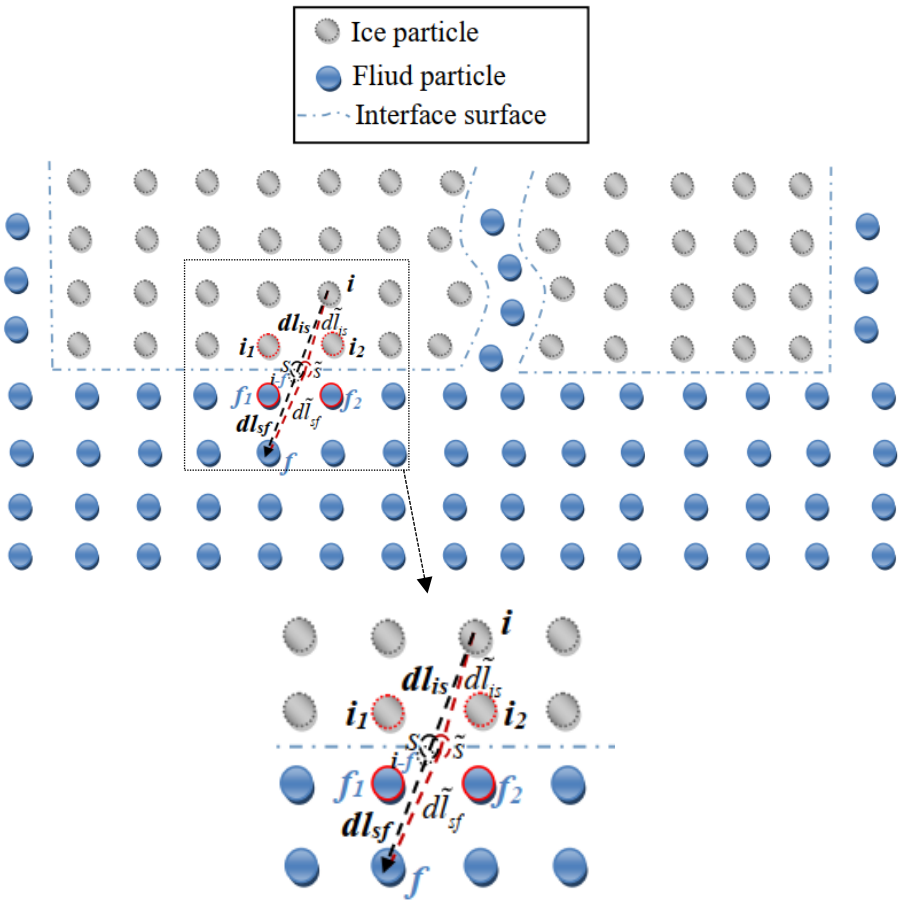

Fig. 5. Interaction between fluid and ice particles at interface boundary: the red circled particles, which are the nearest to the midpoint s of the particle pair *i-f*, are used to approximatively estimate dl_{sf} and dl_{is}.

Based on Eq. (22), we have:

$$\frac{d\boldsymbol{v}_f}{dt}\cdot\frac{\boldsymbol{dl}_{sf}}{\left|\boldsymbol{dl}_{sf}\right|} = -\frac{\left(p_s - p_f\right)}{\rho_f}\cdot\frac{1}{\left|\boldsymbol{dl}_{sf}\right|} + \boldsymbol{g}\cdot\frac{\boldsymbol{dl}_{sf}}{\left|\boldsymbol{dl}_{sf}\right|} \tag{24}$$

where $\boldsymbol{dl}_{sf}$ is a vectorial length along the line of point *s* and the fluid particle *f* (Fig. 5)

and p_s is the pressure at point s, which leads to:

$$p_s = p_f - \rho_f \frac{d\boldsymbol{v}_f}{dt} \cdot \boldsymbol{dl}_{sf} + \rho_f \boldsymbol{g} \cdot \boldsymbol{dl}_{sf} \tag{25}$$

Similarly, according to Eq. (23), we have:

$$p_s = p_{i,dum} + \rho_I \frac{d\boldsymbol{v}_I}{dt} \cdot \boldsymbol{dl}_{is} - \rho_I \boldsymbol{g} \cdot \boldsymbol{dl}_{is} \tag{26}$$

where $\boldsymbol{dl}_{is}$ is a vectorial length along the line of particle i and point s (Fig. 5).

Combining Eq. (25) and (26) gives

$$p_f - \rho_f \cdot \frac{d\boldsymbol{v}_f}{dt} \cdot \boldsymbol{dl}_{sf} + \rho_f \boldsymbol{g} \cdot \boldsymbol{dl}_{sf} = p_{i,dum} + \rho_I \frac{d\boldsymbol{v}_I}{dt} \cdot \boldsymbol{dl}_{is} - \rho_I \boldsymbol{g} \cdot \boldsymbol{dl}_{is} \tag{27}$$

Rearranging it, we obtain:

$$\begin{aligned} p_{i,dum} &= p_f - \rho_f \frac{d\boldsymbol{v}_f}{dt} \cdot \boldsymbol{dl}_{sf} + \rho_f \boldsymbol{g} \cdot \boldsymbol{dl}_{sf} - \rho_I \frac{d\boldsymbol{v}_I}{dt} \cdot \boldsymbol{dl}_{is} + \rho_I \boldsymbol{g} \cdot \boldsymbol{dl}_{is} \\ &= p_f + \rho_f \left(\boldsymbol{g} \cdot \boldsymbol{dl}_{sf} + \frac{\rho_I}{\rho_f} \cdot \boldsymbol{g} \cdot \boldsymbol{dl}_{sf} - \frac{d\boldsymbol{v}_f}{dt} \cdot \boldsymbol{dl}_{if} - \frac{\rho_I}{\rho_f} \frac{d\boldsymbol{v}_I}{dt} \cdot \boldsymbol{dl}_{is} \right) \end{aligned} \tag{28}$$

It is noted that the above expression is obtained by using the fact that the pressure on both side of the interface equals to the pressure on the interface. In addition, according to the kinematic interface condition, we have

$$\frac{d\boldsymbol{v}_f}{dt} \cdot \boldsymbol{e}_l = \frac{d\boldsymbol{v}_I}{dt} \cdot \boldsymbol{e}_l \tag{29}$$

where $\boldsymbol{e}_l$ is the unit vector along the line of s-f in Fig. 5.

Then, substituting Eq. (29) into Eq. (28), we can obtain the following equation:

$$\begin{aligned} p_{i,dum} &= p_f + \rho_f \left(\boldsymbol{g} \cdot \boldsymbol{dl}_{sf} + \frac{\rho_I}{\rho_f} \cdot \boldsymbol{g} \cdot \boldsymbol{dl}_{is} - \frac{d\boldsymbol{v}_I}{dt} \cdot \boldsymbol{dl}_{sf} - \frac{\rho_I}{\rho_f} \cdot \frac{d\boldsymbol{v}_I}{dt} \cdot \boldsymbol{dl}_{is} \right) \\ &= p_f + \rho_f \boldsymbol{e}_l \cdot \left(\boldsymbol{g}(dl_{sf} + \frac{\rho_I}{\rho_f} \cdot dl_{is}) - \frac{d\boldsymbol{v}_I}{dt}(dl_{sf} + \frac{\rho_I}{\rho_f} \cdot dl_{is}) \right) \end{aligned} \tag{30}$$

The pressure $p_{i,dum}$ of particle i due to the action of a single fluid particle f can then be obtained from

$$p_{i,dum} = p_f + \rho_f \left(\boldsymbol{g} - \frac{d\boldsymbol{v}_I}{dt} \right) \cdot \boldsymbol{e}_l (dl_{sf} + \frac{\rho_I}{\rho_f} \cdot dl_{is}) \tag{31}$$

Considering all its neighbour fluid particles, the pressure of the dummy particle is then given by

$$p_{i,dum} = \frac{\sum_{f \in fluid}^{M} p_f W_{if} + (\boldsymbol{g} - \frac{d\boldsymbol{v}_I}{dt}) \cdot \sum_{f \in fluid}^{M} \rho_f \cdot \boldsymbol{e}_l (dl_{sf} + \frac{\rho_I}{\rho_f} dl_{is}) W_{if}}{\sum_{f \in fluid}^{M} W_{if}} \tag{32}$$

where M is the fluid particles which affect the dummy particle concerned. Clearly, it needs to calculate the values of dl_{sf} and dl_{is}. Here, we propose a numerical technique to approximatively estimate dl_{sf} and dl_{is}. Firstly, we identify two ice particles, e.g., i_1, i_2

and the two fluid particles, e.g., f_1, f_2 in the common part of the support domains of particle i and f (Fig. 5), which are the nearest to the midpoint s of the line i-f. If the number of the particles close to the interface in the common part is less than two, i and/or f can be set to be one of i_1, i_2 or f_1, f_2, plus one other ice or fluid particle to ensure 2 ice particles and 2 fluid particles are always identified. Then the position of the midpoint, $\tilde{s}$, of the above four particles can be obtained:

$$\boldsymbol{x}_{\tilde{s}} = (\boldsymbol{x}_{i_1} + \boldsymbol{x}_{i_2} + \boldsymbol{x}_{f_1} + \boldsymbol{x}_{f_2}) / 4. \tag{33}$$

With this, we can calculate the $d\tilde{l}_{is}$ and $d\tilde{l}_{sf}$, which are the distance from particle i to $\tilde{s}$ and the distance from particle $\tilde{s}$ to f, respectively. In addition, $d\tilde{l}_{is}$ and $d\tilde{l}_{sf}$ are assumed to satisfy the following relationship:

$$\frac{dl_{is}}{dl_{sf}} = \frac{d\tilde{l}_{is}}{d\tilde{l}_{sf}}. \tag{34}$$

Apart from these, it is easily obtained that

$$dl_{is} + dl_{sf} = dl_{if}. \tag{35}$$

Combining Eq. (34) and (35) leads to

$$dl_{is} = \frac{d\tilde{l}_{is} \cdot dl_{if}}{d\tilde{l}_{is} + d\tilde{l}_{sf}}; dl_{sf} = \frac{d\tilde{l}_{sf} \cdot dl_{if}}{d\tilde{l}_{is} + d\tilde{l}_{sf}} \tag{36}$$

This numerical technique does not require the explicit information of the interface surface. Furthermore, the way of evaluating dl_{sf} and dl_{is} can be directly extended to complex three-dimensional fluid-structure coupling problems including the broken up in future work. Using Eq. (36), $\frac{d_{bd}}{d_{bf}}$ in Eq. (20) and (21) can be approximated by $\frac{d_{bd}}{d_{bf}} = \frac{dl_{is}}{dl_{sf}}$.

The above derivation is inspired by Adami et al. (2012) for determining the pressure of dummy particles to model solid wall boundaries. Their equation for dummy pressure was given as

$$p_{i,dum} = \frac{\sum_{f \in fluid}^{M} p_f W_{if} + (\boldsymbol{g} - \boldsymbol{a}_b) \cdot \sum_{f \in fluid}^{M} \rho_f \boldsymbol{dl}_{if} W_{if}}{\sum_{f \in fluid}^{M} W_{if}} \tag{37}$$

where $\boldsymbol{a}_b$ is the acceleration of a solid wall. In their derivation, just the kinematic condition (acceleration of a solid wall equal to that of the fluid as in Eq. (16)) was imposed without requesting the pressure on the interface to be the same. Comparing the new equation Eq. (32) with Eq. (37), one can see that the latter is the special case of former, i.e., Eq. (32) reduced to the form of Eq. (37) when $\rho_I = \rho_f$. Our numerical tests

in section 5 show that Eq. (37) does not work well for modelling the problems with large density ratios. It is worthy to point out that the new equation Eq. (32) is not only suitable for simulating the wave-ice interaction, but also for other fluid-structure interaction (FSI) problems even with high density difference between different phases.

4.5. Interacting force treatment for unequal time steps

For the particles near the interface, the momentum equations for fluids and ice should include the interaction forces given in Eq. (18b) and (19), respectively, that is

$$\frac{dv_f^\alpha}{dt} = \frac{F^\alpha_{f\ ice-fluid}}{m_f} + \sum_{j\in fluid}^{N_f} m_j \left(-\frac{p_f + p_j}{\rho_f \rho_j} - \Pi_{fj} \right) \frac{\partial W_{fj}}{\partial x_f^\alpha} + g^\alpha \tag{38}$$

$$\frac{dv_I^\alpha}{dt} = \frac{F^\alpha_{I\ fluid-ice}}{m_I} + \sum_{j\in ice}^{N_I} m_j \left(\frac{\sigma_I^{\alpha\beta}}{\rho_I^2} + \frac{\sigma_j^{\alpha\beta}}{\rho_j^2} - \Pi_{Ij} \cdot \delta^{\alpha\beta} + f_{Ij}^{\ n} \left(R_I^{\alpha\beta} + R_j^{\alpha\beta} \right) \right) \frac{\partial W_{Ij}}{\partial x_I^\beta} + g^\alpha \tag{39}$$

If Eqs. (38) and (39) are solved simultaneously, the interaction forces between the ice particles and fluid particles satisfies the action–reaction principle as discussed previously. When the time step for the fluid is close to that of the structure model, e.g., in Zhang et al. (2019), the interaction forces between the structure particles and fluid particles can be approximately equal to each other in magnitude. However, when the unequal time steps, $\Delta t_f = n\Delta t_I$, are adopted as discussed for Fig. 3, the variables for the ice are updated every time step Δt_I, while the variables for the fluid field are updated only at Δt_f. It means that the forces exerting on the ice particles from fluid particles are updated at each of time steps Δt_I, while the forces from the ice particles on the fluid particle are updated only at Δt_f. As a result, the interaction forces between the fluid and ice particles cannot be equal in magnitude because of the asynchronous updating, which will cause larger errors in computations.

In order to rectify this problem, a treatment is proposed here. In this treatment, when executing the ice solver at the time step t^k (Fig. 3), the force on the ice particle from fluid particles $F^\alpha_{I\ fluid-ice}$ in Eq. (19) is calculated using the variables at t^k. Then this force is kept unchanged at following time steps $t^k + \Delta t_I$, $t^k + 2\Delta t_I$, ….. $t^k + (n-1)\Delta t_I$ until the next time step $t^k + n\Delta t_I$ (Fig. 3). At this time, the fluid field variables are updated using the ice variables at $t^k + n\Delta t_I$. The process then continues to the next time steps. The numerical analysis in Section 5.1 shows this treatment can lead to better results than updating the interaction force at each step for ice simulation.

4.6. Separation model of ice particle breakup

After breakup of ice floe, the two smaller ice pieces (Fig. 6) will lose their interaction physically. But in the SPH algorithm, the particles on both sides of the crack may still interact with each other if they are in support domain (Fig.6a), which will add unphysical contributions to the particles. Therefore, we need to find an effective

technology to solve this problem. There are two issues about this. One is how to identify if the particles are separated by the crack, and the other is how to deal with the equations of the identified particles. The second issue can be addressed straightforwardly, i.e., just removing their interaction. The first issue will be addressed in the following paragraphs.

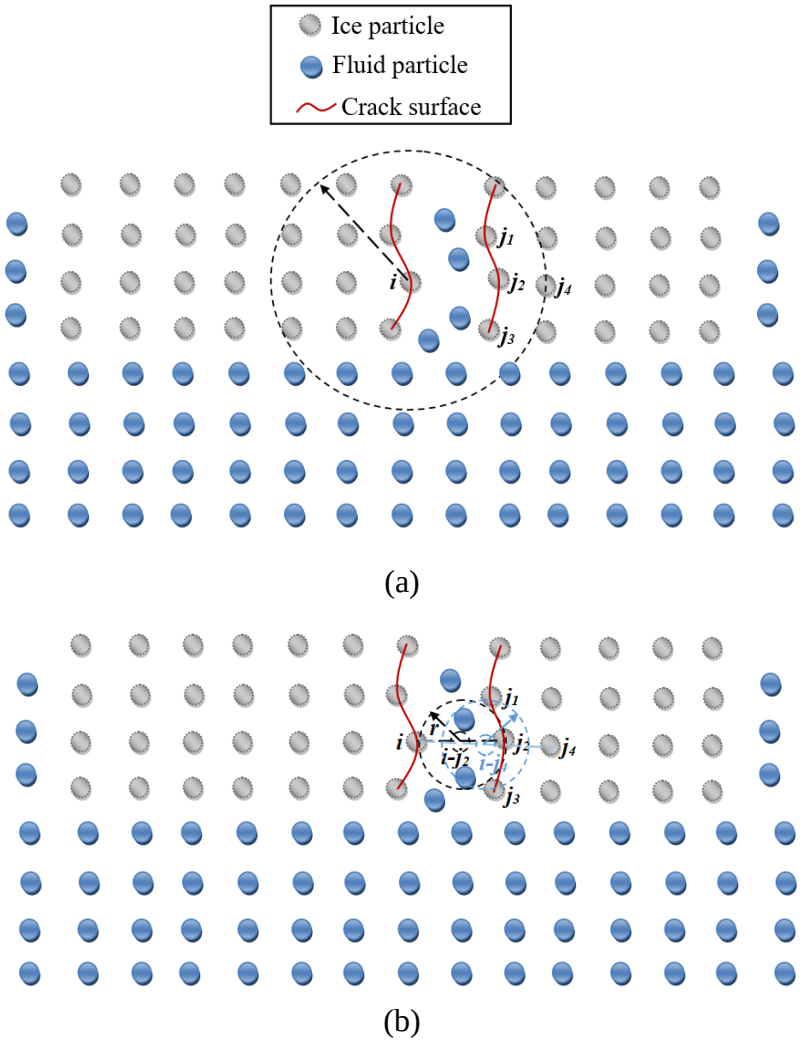

Fig. 6. A schematic diagram of fluid and ice particles after breakup.

To identify if particles are separated by a crack, an auxiliary function, which is inspired by the interaction model employed in peridynamic method (Silling and Askari, 2005), is used and defined as:

$$ST = |\boldsymbol{\xi}+\boldsymbol{\eta}| - |\boldsymbol{\xi}| \tag{40}$$

where $\boldsymbol{\xi}=\boldsymbol{x}'-\boldsymbol{x}$ is the initial relative position between two particles with their positions at $\boldsymbol{x}$ and $\boldsymbol{x}'$, respectively; $\boldsymbol{\eta}=\boldsymbol{u}(\boldsymbol{x}',t)-\boldsymbol{u}(\boldsymbol{x},t)$ is the relative displacement between the two particles at time t with $\boldsymbol{u}(\boldsymbol{x},t)$ being the displacement of the particle at $\boldsymbol{x}$, $\boldsymbol{\xi}+\boldsymbol{\eta}$ represents the relative position between particles at the current time t. When

the value of ST is larger than a critical value, the concerned particles are judged as separated by a crack.

There will be two scenarios associated with identifying the breakup. The first scenario is where some fluid particles penetrate the crack while in the second one there is no fluid particle in the crack. To consider the different scenarios, the following two steps are followed:

(1) Check if $ST>ST_0$ with $ST_0=\begin{cases}0.5\cdot dx & |\xi|>1.0\cdot dx\\ 0.55\cdot dx & |\xi|\le 1.0\cdot dx\end{cases}$, where dx is the initial particle spacing. If no, there is no crack. If yes, check will be further performed to find if there is any fluid particle between the pair, such as i and j_2 in Fig. 6(b). For doing so, a virtual point at the midpoint of this particle pair and its sub-domain of r=1.5dx are looked at. If there are fluid particles in the sub-domain, it is determined that this particle pair i and j_2 are separated by fluid particles and so a crack has appeared. If no fluid particles are found in the domain, perform the next step.

(2) Check if ST>1.0dx after performing the previous step without finding any fluid particles between the pair. If no, there is no crack. If yes, the pair of the ice particles concerned is judged as separated by a crack.

For all the pairs of the particles judged as separated by a crack, the interaction between them will be completely removed.

The above proposed method does not require explicit information about the geometry of the ice floe. Thus, it is easy to implement and has a potential to be extended to dealing with complex three-dimensional fluid-ice coupling problems in future.

5. Numerical results and discussions

5.1. Breaking of ice floe by regular waves

In this section, the breakup of ice floe induced by regular waves is simulated. Main purpose here is to carry out convergent tests for finding suitable number of particles to be used, validate the numerical results by experimental data available and show the evidence that the new numerical techniques proposed in this paper work well.

As shown in Fig. 1, the length of wave tank is 24 m, the initial still water depth is D = 0.4 m. The ice floe floating on the water surface has density ρ = 890 kg/m^3 and Poisson's ratio υ = 0.33. According to Zhang et al. (2017), the friction angle is selected to be 36^o and the dilatancy angle φ one-third of the friction angle ($\varphi = \phi/3$). Regular waves are generated by using a piston wavemaker. The motions of the wavemaker can be found in the Gotoh et al. (2004). The other parameters for the ice floes and wave conditions used in the numerical tests are given in Table 1, unless mentioned otherwise.

It is noted that in Table 1 and hereafter, a length scale is nondimensionalised by the water depth D and the time by $t \to t\sqrt{g/D}$. The parameters selected in this section is based on Wang et al. (2000), whose experimental results will be used for the validation.

Table 1 Parameters for ice floe and regular wave.

Parameters	Case A	Case B
Elastic modulus of ice E (MPa)	138.65	18.5125
Flexural strength of ice σ_f (kPa)	29.5	12.5
Length of ice floe L_i	3.75	2.00
Thickness of ice floe th_i	0.05	0.05
Wave height (H)	0.0375	0.1
Wave period (T)	5.94	7.43
Ratio of ice length to wavelength	0.77	0.31

5.1.1. Convergent tests

The convergent tests are carried out for Case A, potentially requiring more particles. For these tests, the initial particles are uniformly distributed but the number of particles is varied. The simulation proceeds to the time after the ice floe has broken up. The numerical results of the fracture length measured from the left edge of ice floe to the breaking point are presented in Fig. 7 with N being the different total particle numbers for water and ice. In Fig. 7(a), the blue colour represents the water particles while the other colours denote the level of accumulated plastic strain ($\bar{\varepsilon}_p$ defined in Appendix A) of ice particles. The relative error Er_l presented in Fig. 7b is calculated by $Er_l = |l_0 - l|/l_0$, where l is the computed fracture length and l_0 is the corresponding length from experimental data given by Wang et al. (2000). The figure shows that the numerical fracture length becomes closer to the experimental value and the error is reduced with the increase of particle numbers. One can see from the figure that the reduction rate of the error become quite small when the particle number increases from N = 216675 (Log(N)~5.3) to N = 601875 (Log(N)~5.8). The results corresponding to N = 385200 are then considered to be convergent. The initial particle size, i.e, dx_i = dx_f = 0.0125 corresponding to N = 385200 will be adopted in the following sections.

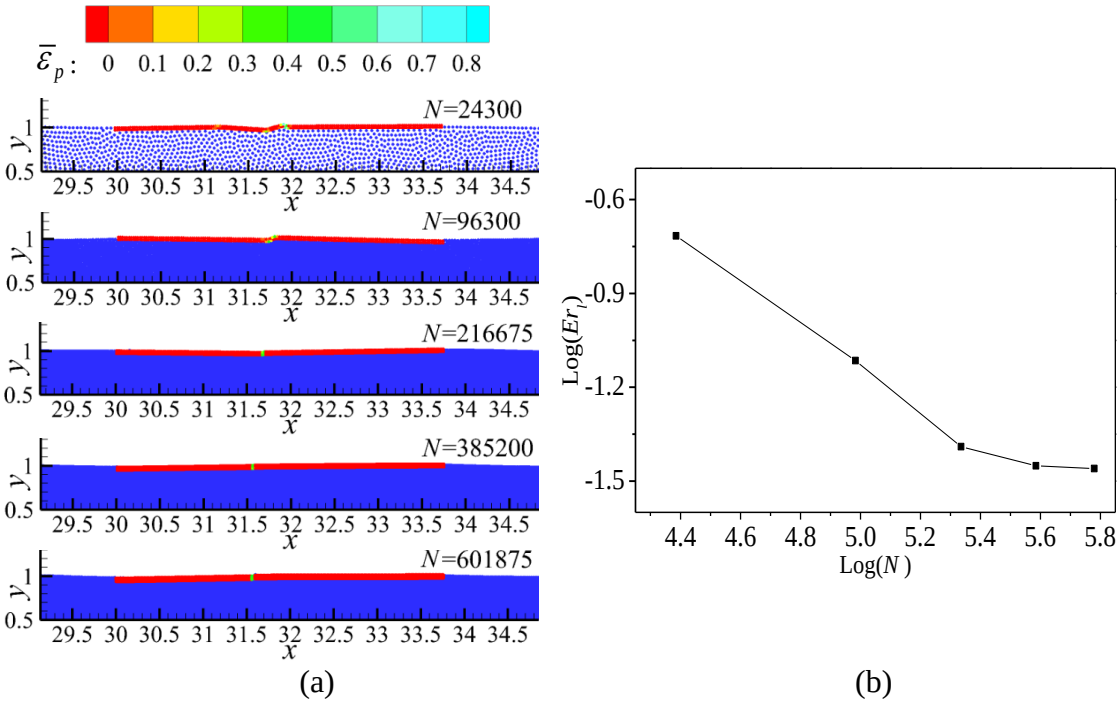

Fig. 7. The fracture length obtained by using different number of particles: (a) particle configuration after the breakup observed; (b) relative error in the fracture length

5.1.2. Comparison with experimental results

In this subsection the numerical results will be compared with the experimental data by Wang et al. (2000). The wave-induced breakups of model ice floes under different conditions are considered.

The fracture length is first examined. For this purpose, Case A and B given in Table 1 are simulated by using the numerical method with N = 385200. The configurations at three-time steps after the breaking up are shown in Fig. 8 for Case A and in Fig. 9 for Case B, respectively. Same as in Fig.7, the blue colour represents the water particles while the other colours denote the level of accumulated plastic strain of ice particles. It can be seen that the accumulated plastic strain is quite large at the breaking point while it is near zero in other parts of the ice floe, indicating that the quantity is a good indicator for the breaking point. The fracture lengths obtained by the numerical method are compared in Table 2 together with the experimental data from Wang et al (2000). It is noted that the experimental values in the table are different from those of Wang et al (2000). That is because they are nondimensionalised here while they are dimensional in the reference. The relative errors between the experimental and numerical results are also presented in the table. It can be seen that the error of the numerical results is less than 4.5%, which is considered to be acceptable. It is noted that the fracture section of the ice floe is largely normal to the propagation direction of waves in the experiment and so the response of the ice floe to the waves can be considered approximately as two-dimensional.

That is the reason why our numerical method can match acceptably with the experimental data in Wang et al (2000).

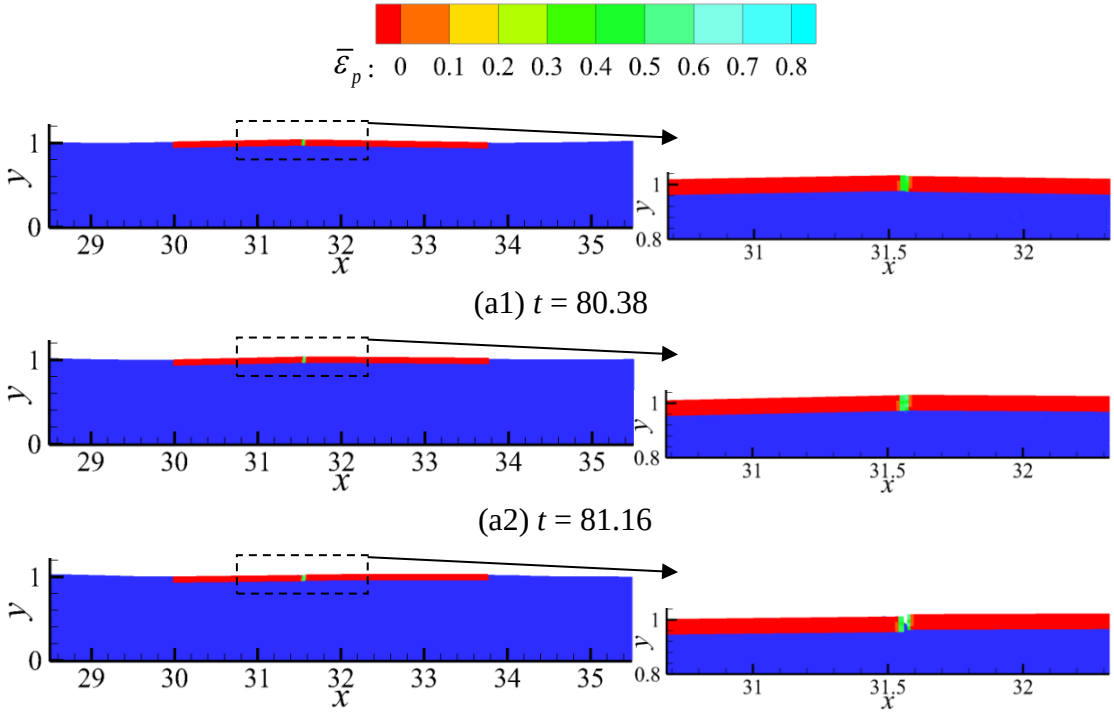

(a1) t = 80.38

(a2) t = 81.16

(a3) t = 81.94

Fig. 8. Particle configurations of ice floe after breakup is observed (Case A)

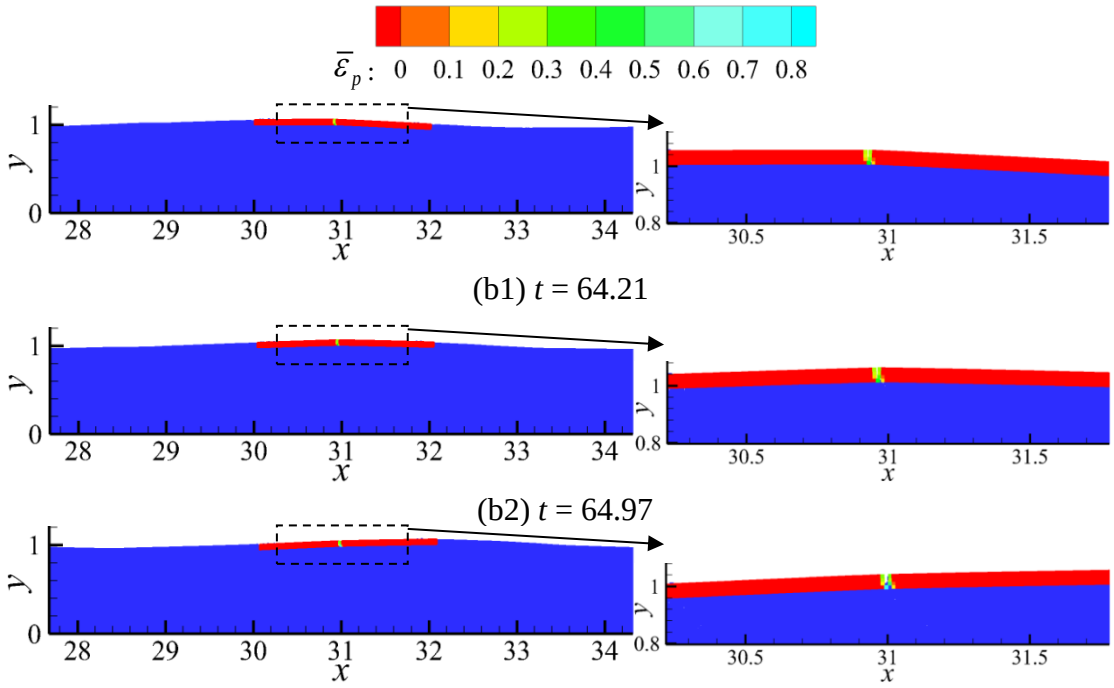

(b1) t = 64.21

(b2) t = 64.97

(b3) t =65.91

Fig. 9. Particle configurations of ice floe after breakup is observed (Case B)

Table 2 Fracture lengths.

Case	Experimental data	Numerical lengths	Relative error
A	1.625	1.5675	3.54%
B	0.875	0.9125	4.29%

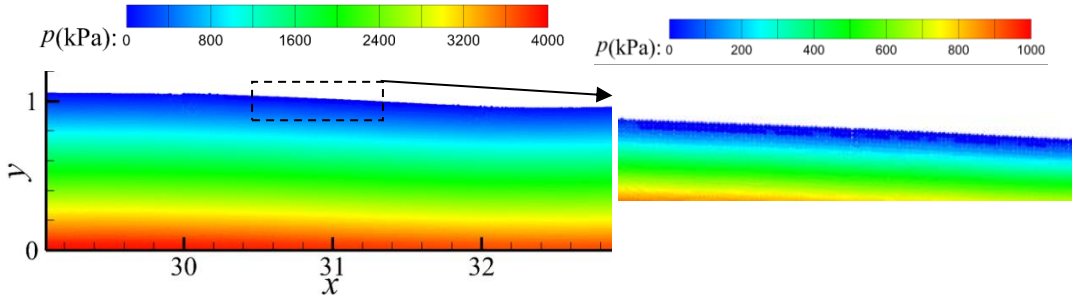

(a1) t = 63.15

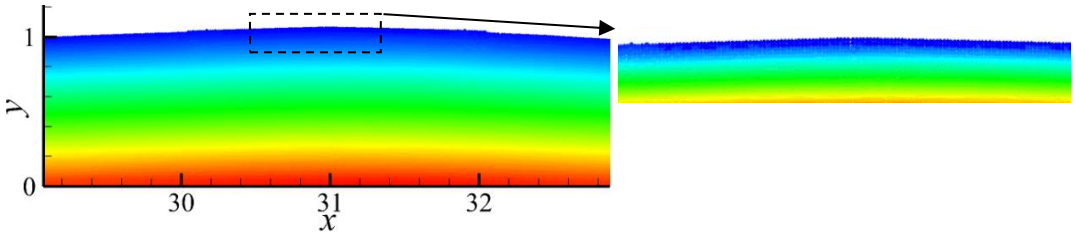

(a1) t = 64.97

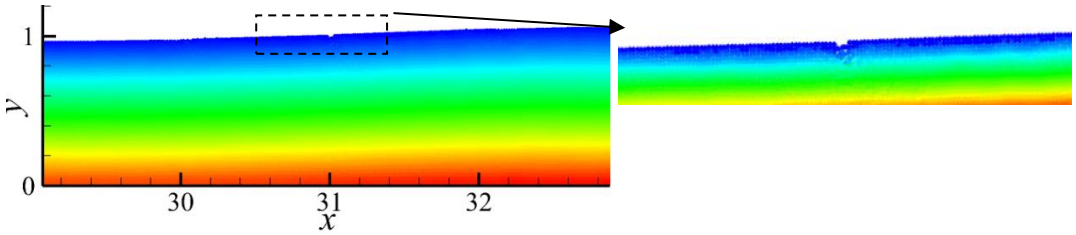

(a1) t = 66.93

Fig.10. Snapshots illustrating distribution of particles along with pressure field

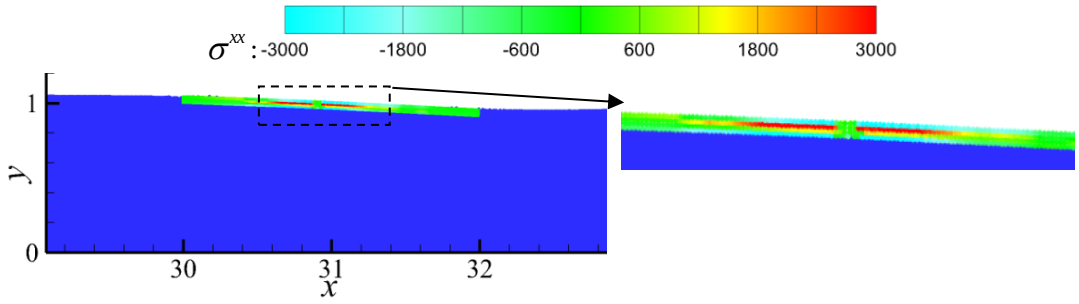

(a1) t = 63.15

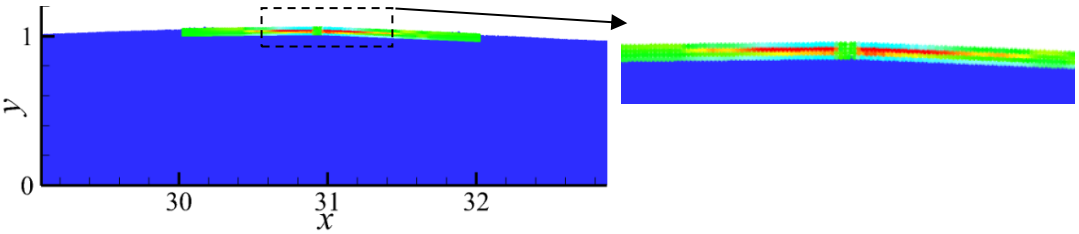

(a1) t = 64.21

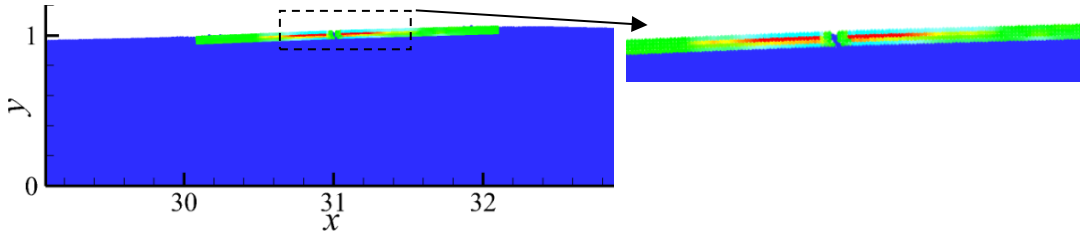

(a1) t = 66.31

Fig.11. Snapshots illustrating distribution of particles along with stress field of ice floe

Fig. 10 shows the spatial distribution of pressure in Case B. From Fig. 10, the developed wave-ice interaction method can provide quite smooth and consistent pressure fields particularly near the interface. Fig. 11 shows the stress distribution for the ice floe in Case B. As illustrated by this figure, the stress fields of ice floe are reasonably smooth as well.

The total displacement (Y_m) of the ice floe is then examined. For this purpose, the displacement is measured from a trough to a peak in the time history of the ice heaving motions at its middle, and averaged over a few periods. The parameters for the cases here are the same as those in Case A and Case B except for the incoming wave height. Fig. 12 depicts the comparison of the numerical displacement and the experimental data.

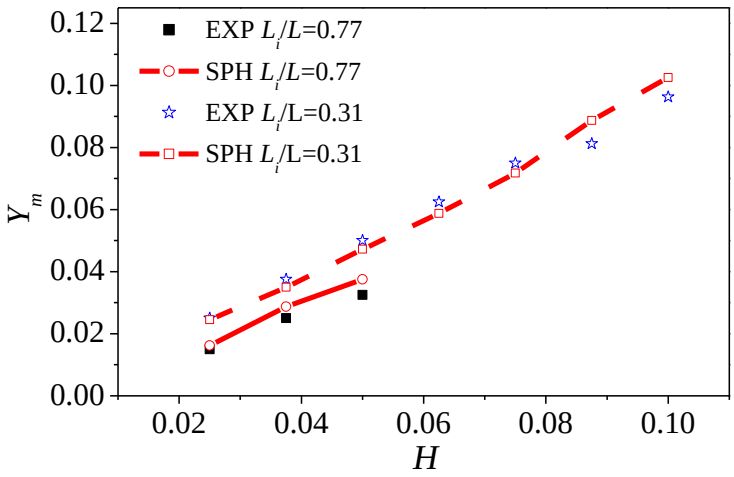

Fig. 12. Comparison of maximum heave displacements in middle of floe of SPH results with experimental data with different L_i/L.

In general, the displacement Y_m increases with the wave height. Under the same wave height, the smaller value of L_i/L leads to larger displacement Y_m. Overall speaking, the present simulation gives the results which are quite close to the experimental data, though there are some visible discrepancies.

The minimum wave height H_{min} leading to the ice floe breaking is examined next. To obtain the values of H_{min} and compare them with the experimental data, the specific cases associated with Fig. 4 in Wang et al (2000) are considered. The parameters for

the cases are given in Table 3. For each case, the numerical simulations are sequentially carried out for different values of $\rho gH/\sigma_f$ with an increment of 0.0025. The value leading to an accumulated plastic train of about 0.1 is considered to be the minimum wave height H_{min} generating breakup. Fig. 13 shows the nondimensional minimum wave heights in terms of $\rho gH_{\min}/\sigma_f$ versus the ratio of ice floe length to the wavelength L_i/L, in which the numerical results are denoted by 'SPH' and the experimental data presented by Wang et al (2000) denoted by 'EXP'.

Table 3 Parameters of different cases.

th_i/L	Case ID	Length of ice floe L_i	Wave period T	Elastic modulus E (MPa)	Flexural strength σ_f (kPa)
0.0133	C	3.75	5.94	234.8856	60.6
	D	3.75	7.43	234.8856	60.6
0.025	E	1.9	7.43	18.824	13.68
	F	2.0	4.95	25.896	15.6
	G	2.0	5.94	21.528	15.6
0.0328	H	1.65	4.95	22.07	29.48
	I	1.5	3.47	25.9458	16.6

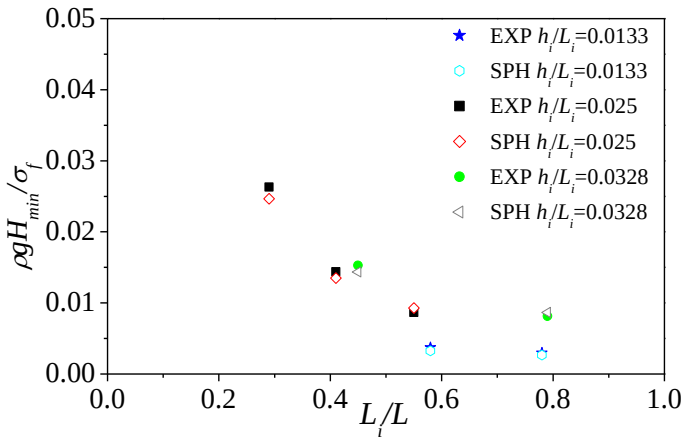

Fig. 13. Comparison of the minimum wave height $\rho gH_{\min}/\sigma_f$ versus the L_i/L between numerical results and experimental data.

It can be seen from Fig. 13 that the minimum wave height decreases with the increase of L_i/L. For the similar value of L_i/L, such as these near 0.8, the corresponding minimum wave height increases with the increase of th_i/L. It is also found that the numerical minimum wave heights are in quite good agreement with the experimental data.

In summary, the comparisons of fracture length, the heaving motion and minimum

wave height for breaking up described in this sub-section demonstrate that the numerical method presented in the paper can give reasonably good results close to experimental data.

5.1.3 Volumetric strain rate $\dot{\varepsilon}_{ev}$ of ice

It has been indicated in Section 2.2.2 that the constitutive model depends on strain rate. To justify the constitutive model used this paper, the volumetric strain rate $\dot{\varepsilon}_{ev}$ of the ice near the breaking point is given in Fig. 14 for Case A and Case B. It shows that the maximum strain rate is about 0.02 1/s for Case A and 0.05 1/s for Case B, respectively. This indicates that the failure of ice is at high strain rates (higher than 0.001 1/s). At this relatively high strain rate, the failure mode should be brittle (Schulson, 2001) and so the visco-plastic effect is weak. Therefore, it is reasonable to use the elastic-plastic constitutive model for the simulation of wave-induced breakup of the ice floe in this paper.

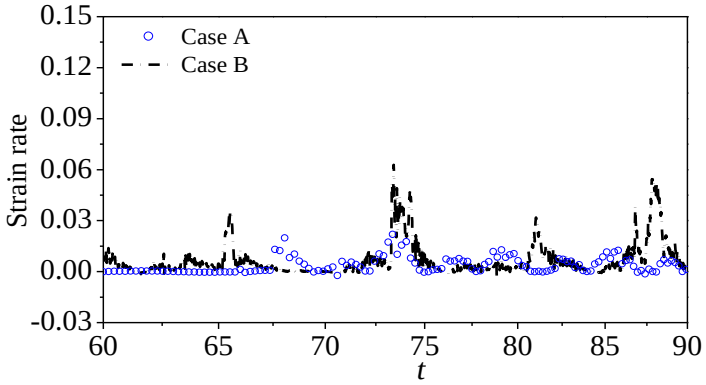

Fig. 14. Time history of the volumetric strain rate of ice near breaking point

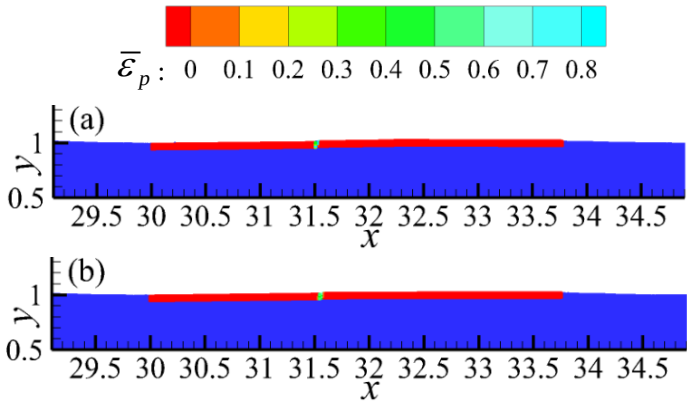

Fig. 15. Comparisons of fracture lengths for wave-induced breakup of ice floe obtained by (a) using Eq. (37) and (b) Eq. (32) both at t = 81.16

5.1.4. Effect of new formulation for pressure of the dummy particle

In Section 4.4, a new method, Eq. (32), for determining the pressure on dummy particles to correctly model wave-ice interaction is proposed, which explicitly includes

a term associate with density ratio, compared to the existing formulation Eq. (37). Its effectiveness will be shown in the section. For this purpose, Case A is simulated using Eq. (32) and Eq. (37) respectively, in which the density ratio is 0.89. The fracture lengths are illustrated in Fig. 15. Compared with the experimental results discussed above, the error in fractur length predicted by using Eq. (32) is 3.54% while it is 6.77% by using Eq. (37). The difference is not much for this case as the density ratio is not very far from 1.

To further demonstrate the effectiveness of Eq. (32), another case with a large density ratio of 0.1 is considered by using the two different formulations. All other parameters are the same as for Fig. 15. The deformations of ice obtained by using Eq. (32) and (Eq. (37) are depicted in Fig. 16. One can observe that the deformation of ice predicted by Eq. (37) looks to be unreasonable and non-physical with the lower part of ice having a quite large strain rate and being discontinuous with the upper part of ice. In addition, the simulation process collapsed immediately after $t = 0.134$. In contrast, the reasonable deformation obtained by using Eq. (37) is observed in Fig. 16(b). This demonstrates the new formulation given in Eq. (32) can be used for modelling wave-structure problems with the large density difference.

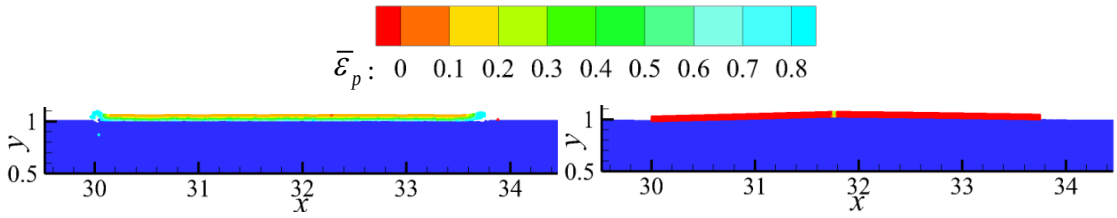

Fig. 16. Comparisons of ice deformation simulated by (a) using Eq. (37) at $t = 0.134$ and (b) Eq. (32) at $t = 75.0$

5.1.5. Effect of interacting force treatment for unequal time steps

A simple treatment for the force on the ice particle by its neighbouring fluid particles $F^{\alpha}_{I\ fluid-ice}$ for unequal time steps was introduced in Section 4.5. To demonstrate its effectiveness, Case A is simulated with or without applying the treatment using the same parameters for Fig. 8. The configuration of particles with applying the treatment has been shown in Fig. 8. The configuration without applying it is similar, but the fracture length is different. If the treatment is not applied, the fracture length is 1.462 and its error compared with experimental data is 10.07%. They are significantly different from these obtained by applying the treatment as given in Table 2, where we have seen that the fracture length is 1.5675 and the error is only 3.54%. This demonstrates that the simple treatment given in Eq. (39) can significantly improve the accuracy of numerical results.

5.1.6. Effect of Separation model of ice particle breakup

Section 4.6 proposed a new separation model of ice particles after they breakup. The effectiveness of the model will be examined in this section. For this purpose, Case B is simulated with or without applying the model using the parameters for Fig. 9. Fig. 17 gives the comparison of the numerical results at three-time instants. The results in Fig. 17(b) with applying the model show that after the ice breaks up, the two pieces split farther and water comes in between them, which is reasonable. However, the results in Fig. 17(a) without applying the model do not fully reflect the reasonable phenomenon. In particular, the ice pieces become somewhat reconnected at t = 70.09 after the two pieces are separated by water at t = 68.82. Physically, this is not correct. This investigation confirms that separation model of ice particle breakup does work and work reasonably well.

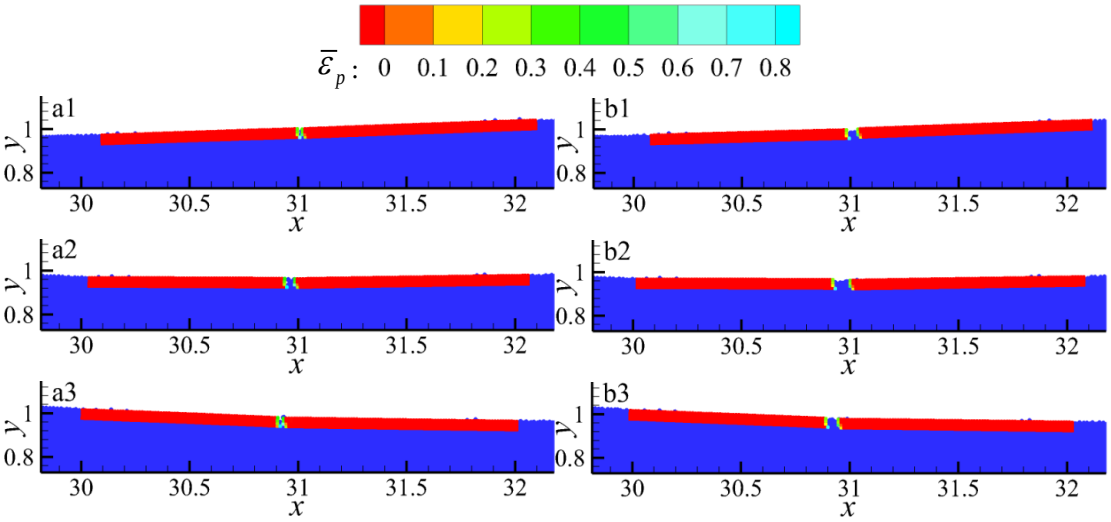

Fig. 17. Wave-induced breakup of the ice floe: (a) without applying the separation model; and (b) applying the separation model at different time instants: t = 66.93 (a1 and b1); t = 68.82 (a2 and b2); t = 70.09 (a3 and b3)

5.2. Breakup of ice floe induced by solitary waves

In this part, the breakup of an ice floe caused by a solitary wave is discussed. The solitary wave is generated by using piston wave maker in the same way as in Ma and Zhou (2009). The size of the numerical tank and relevant parameters of ice floe are the same as those in Case A except for these of waves. Different wave heights will be considered.

Fig. 18 gives the comparison of the failure process of the ice floes under different wave heights (H = 0.15, 0.225 and 0.3). Fig. 18(a) depicts the deformation of ice floes when the solitary wave crest is about at their middle. Fig. 18(b) shows the deformation when the wave crests near the right end of the ice floes while Fig. 18(c) gives the deformation when the wave crest propagates to a point at a distance of about one ice-length after its right end. The corresponding times are different in the figures because

the wave propagating speeds are different for different wave heights. This figure shows that the ice floes first undergo the upward bending in middle part under the solitary wave crest and begin to failure. Then they become broken. After that the broken ice pieces are separated from each other and slightly drifts downstream. The distance drifted increases with the wave hights. In addition, the overtopping of water on the ice floes can be observed, in particular in the cases for the larger heights. The figure also shows that the ice floe is likely to break into more pieces with the increase in the wave height. The length of each piece is not significantly different.

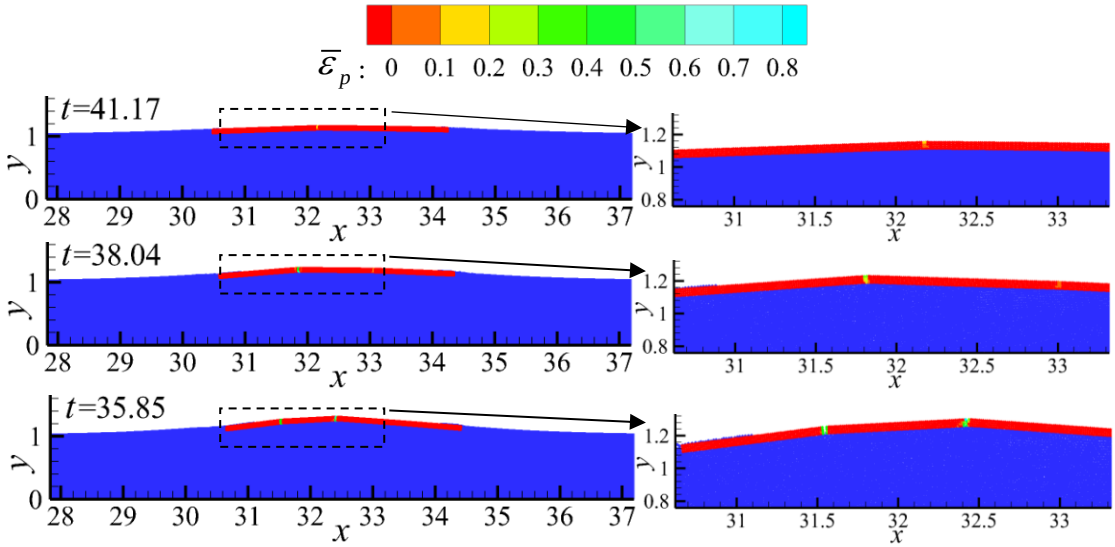

(a) Ice deformation when wave crest is near the middle of ice floes

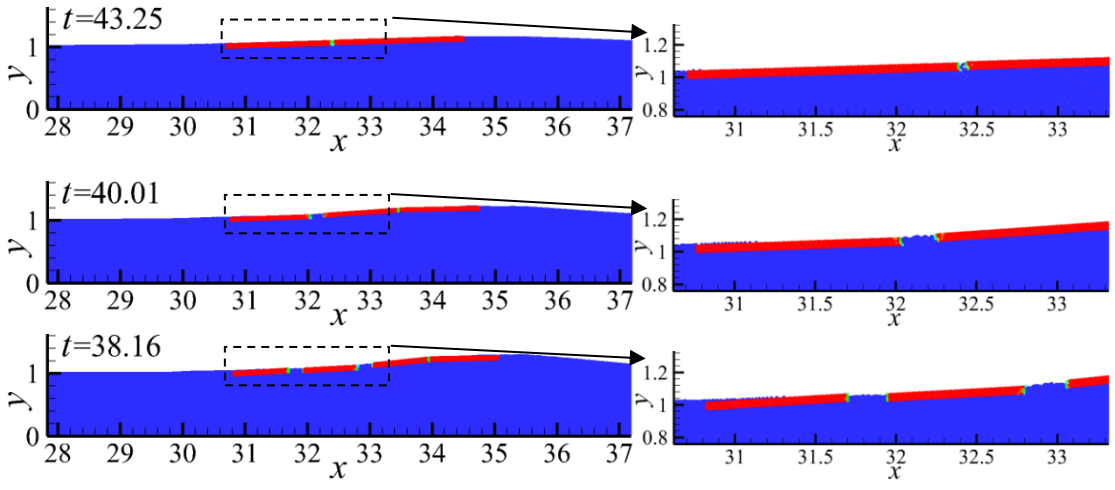

(b) Ice deformation when wave crest is near the end of ice floes

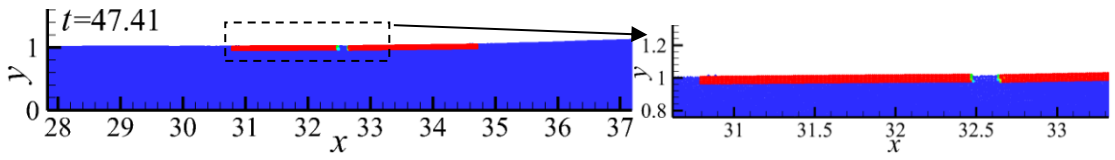

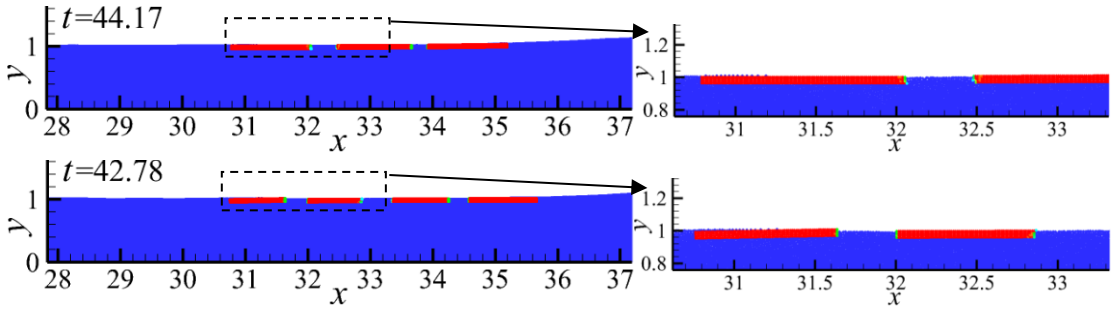

(c) Ice deformation after wave crest passes ice floes

Fig. 18. Comparison of failure process of ice floe in solitary waves with different wave heights. In each subplot, H = 0.15, 0.225 and 0.3, respectively, from top to bottom)

To further illustrate the broken ice behaviour, the relationship between the length of the first ice piece L_f at the upwave side and wave height H is shown in Fig. 19. Overall, the values of L_f is decreasing with the increasing of solitary wave height. And the length L_f decreases rapidly before H = 0.225, then the rate of decrease slows down when the wave height H >0.3. However, at the wave height of 0.275, the length is significantly larger than others. We also carried out simulations of the cases with the wave height being 0.24 and 0.25 (not shown in here) and obtained similar L_f as 0.275. This point needs to be further investigation in future work.

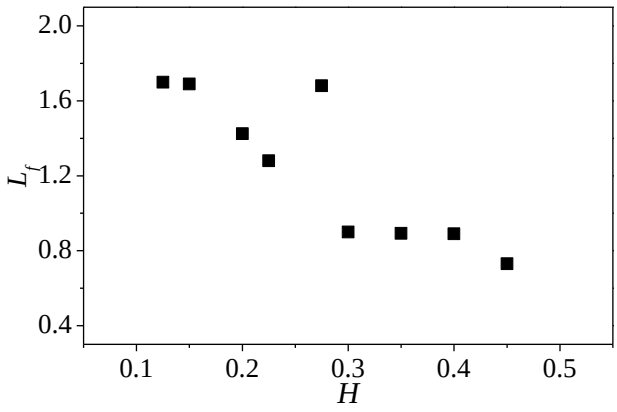

Fig. 19. Length of first ice piece at upwave side L_f via wave heights.

5.3. Breakup process of ice floe induced by focused wave groups

Extreme wave events occur in many places including deep water and shallow water. Such events are often modelled by using a focused wave group. In this section, a study is carried out on the breakup process of ice floe induced by focused wave groups.

Firstly, the numerical method described in this paper is validated for the case of simulating the focused waves only by comparing its results with experimental data in Baldock et al. (1996). The focused wave group is generated by using a piston wavemaker in the same way as that in Ma (2007). The displacement of the wavemaker is given by summing 29 wave components of equal amplitude. The focus point is set to

be 20.0 from the wave maker and the focus time is set to be 56.95, respectively. Fig. 20 gives the comparisons of the time history of the focused wave elevations at the focus point between the experimental data and the numerical results for different specified amplitude A_f. Because the actual focal time differ for different value of A_f (Baldock et al., 1996; Westphalen et al., 2012), the focal time are all shifted to zero to compare with one another in the Fig. 20. It can be seen that the numerical results agree well with those measured in the physical tank tests although there is slight underestimation at the wave crests.

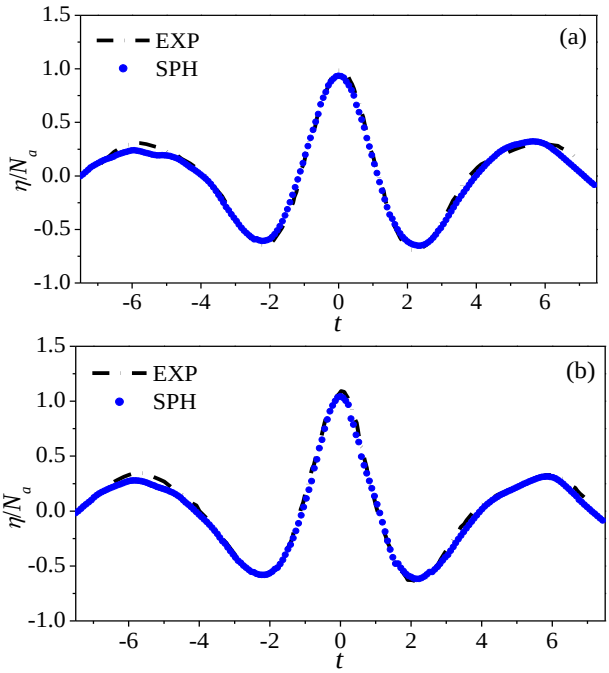

Fig. 20. Time history of the wave elevation at the focal point: (a) A_f = 0.055; (b) A_f = 0.095.

Secondly, the breakup of ice floe induced by the focused wave group is studied. The focused waves are generated in the same way in Fig. 20 but the focal point and focal time is set to be 25 and 100, respectively. The middle of the ice floe is initially set at the focal point. The relevant parameters of ice floe are the same as those in the Case A described above but the length of ice floe may be changed when necessary.

The breakup of ice at different time instants under different wave amplitudes are illustrated in Fig. 21. Fig. 21(a) shows that the ice floe fails in bending before the focal time. The wave overtopping on the ice floe at the left end can be observed like what has been observed in Fig. 18 for solitary waves. As shown in Fig. 21(b), when the wave groups focus approximately near the focal point, the ice floe breaks up particularly in the case with larger wave amplitudes. Especially, there is always a crack near the specified focal point. With the focused wave group continues to move forward and pass through the ice floe, the breaking ice pieces are separated from each other as shown in Fig. 21(c). In addition, for the case with larger wave amplitude, the ice floe is broken

into shorter but more pieces.

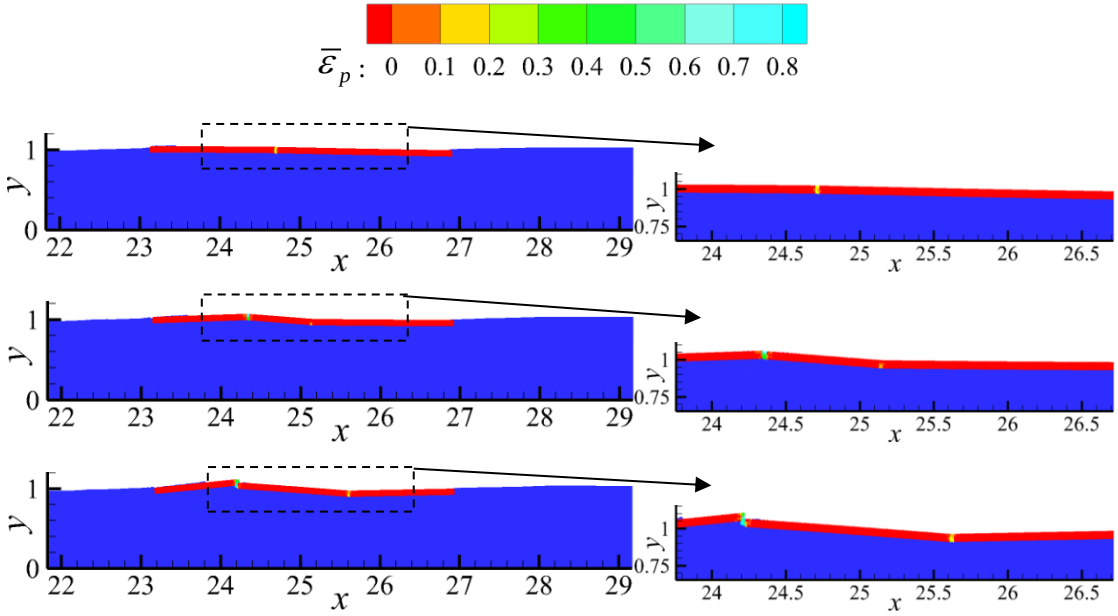

(a) t = 97.06

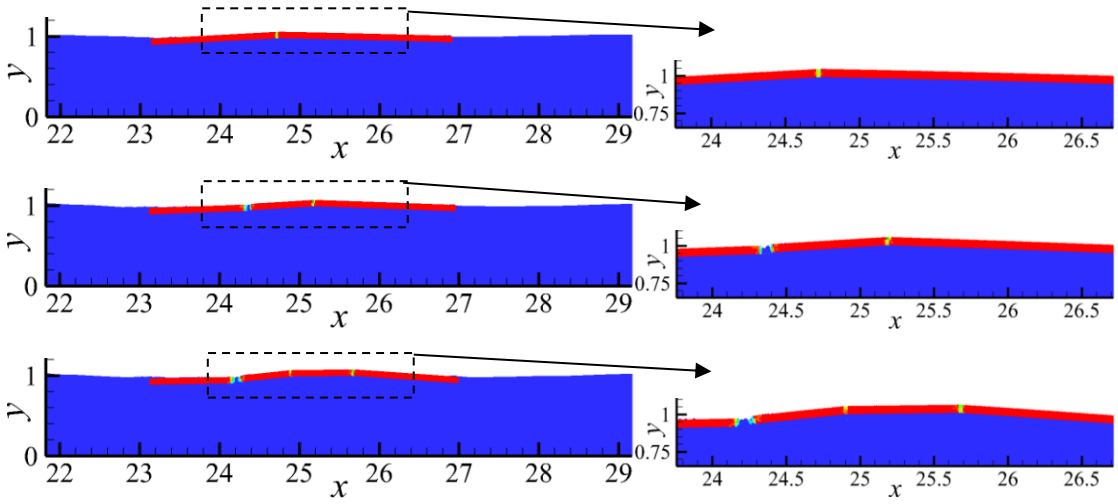

(b) t = 99.05

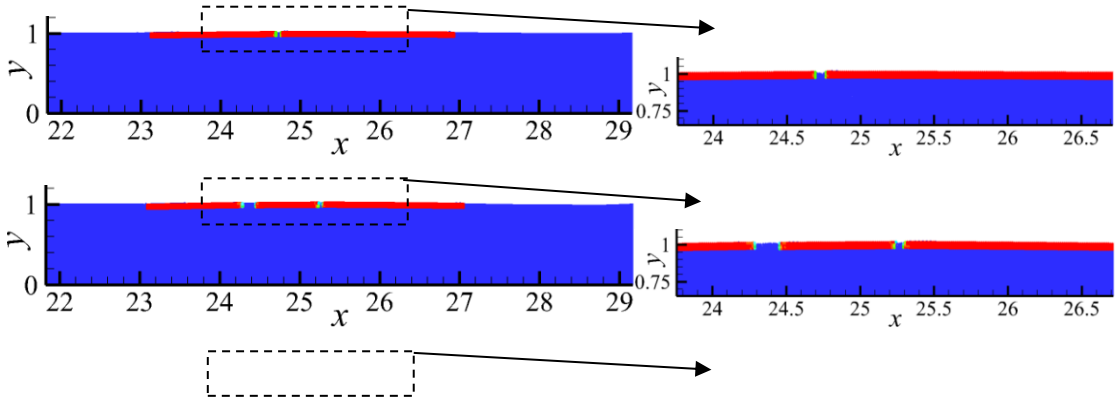

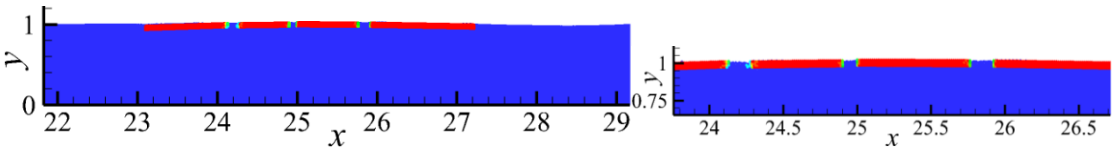

(c) t = 110.93

Fig. 21. Comparison of breakup process at different time instants under different wave amplitudes (from top to bottom for each instant: A_f = 0.05, 0.075 and 0.1 respectively)

To further examine how the wave amplitude affects the number of fragmented ice pieces after ice floes are broken, the cases with a range of wave amplitudes and with different ice length are simulated. The results are shown in Fig. 22, in which N_f denotes the fragmented number of ice. As can be seen, the number of fragmented ice pieces generally increase with the increase of the wave amplitude. In addition, the larger the length L_i of ice floe is, the more pieces the ice floe breaks into under the same wave amplitude. Compared with the cases for solitary waves, the ice floe is easier to be broken and broken into more pieces under the action of the focused wave groups.

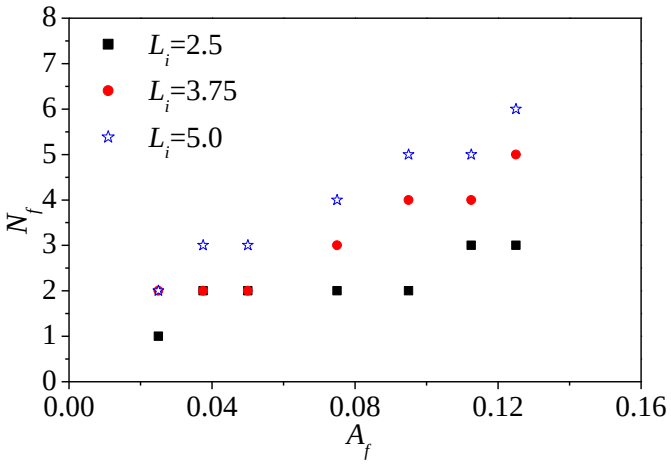

Fig. 22. Comparison of the number of ice pieces under the different length of ice floe and the different wave amplitude A_f.

Conclusion

This paper presents a new numerical method for simulating wave-ice interaction with possible breakup of ice. Two-way coupling approach is adopted, i.e, both effects of water on ice and ice on water are considered. The method is based on the SPH method but several new numerical techniques are developed to address the challenges associated with wave-ice interaction. These include a new model for dealing with the interaction between the fluid and ice. In this model, the kinematic and dynamic conditions on the interface between ice and fluid are considered, and the density difference between ice and fluid is taken in account. These also include a separation model for dealing with breakup of ice. The separation model is easy to be implement

and may be extended to deal with three dimensional problems. Apart from these, to improve the computational efficiency, an unequal time-step scheme for simulating ice and fluid is adopted and the problem caused by the unequal time-step scheme is rectified by a simple but effective treatment.

The numerical method is validated by experimental data available in literature. The heave displacement of ice, the fracture length of broken ices and the minimum wave height which causes ice breakup under action of regular waves are examined. Various parameters are considered, including different wave heights, different wave lengths, different physical properties of ice and different lengths of ice floes. In all the cases examined, the numerical results agree satisfactorily with experimental data. Numerical studies are also carried out on the effectiveness of the new techniques developed in this paper. These studies demonstrate that the techniques work well in simulating wave-ice interaction, and particularly the breakup of ice in waves.

The numerical method is employed to model the interaction of ice floes with solitary waves and focused wave groups. It has been found that the length of broken ice piece decreases with the increase of solitary wave height. However, the length does not change significantly when the wave height is large enough, such as >0.3 for the cases studied. For the cases associated with focused waves, it is found that there is always a crack near the specified focal point. It is also found that the ice floe is easier to be broken and broken into more pieces under the action of the focused wave groups than solitary waves, even subjected to waves with smaller height. As far as we know, there has been no study on the ice breaking behaviours caused by solitary and focused waves. Nevertheless, these results associated with solitary and focused waves need to be validated by experiments, which are now unavailable in public domain.

The numerical method may be extended to three dimensional problems in future studies.

Acknowledgements

The authors at City, University of London gratefully acknowledge the financial support of EPSRC projects (EP/T026782, EP/T00424X and EP/V040235). A part of the work was done when the 1st author studied in Harbin Engineering University.

Appendix A. Equations of the ice constitutive model and cohesion softening

A.1. Elastoplastic constitutive equation of ice

According to Bui et al. (2008) and Deb and Pramanik (2013), the stress tensor $\sigma^{\alpha\beta}$

in the elastic-plastic ice model is firstly estimated by:

$$\hat{\sigma}^{\alpha\beta} = \int \dot{\sigma}^{\alpha\beta} d\sigma \tag{A.1}$$

where the stress rate of the tensor $\dot{\sigma}^{\alpha\beta}$ is defined by:

$$\dot{\sigma}^{\alpha\beta} = \begin{cases} 2G\dot{e}^{\alpha\beta} + K\dot{\varepsilon}^{\gamma\gamma}\delta^{\alpha\beta} & \text{if } F(\sigma^{\alpha\beta}, c) < 0 \text{ (elastic)} \\ 2G\dot{e}^{\alpha\beta} + K\dot{\varepsilon}^{\gamma\gamma}\delta^{\alpha\beta} - \dot{\lambda}\left(\bar{\eta}K\delta^{\alpha\beta} + \dfrac{G}{\sqrt{J_2}}s^{\alpha\beta}\right) & \text{else (plastic)} \end{cases} \tag{A.2}$$

in which $\dot{e}^{\alpha\beta} = \dot{\varepsilon}^{\alpha\beta} - \frac{1}{3}\dot{\varepsilon}_{ev}^{\gamma\gamma}\delta^{\alpha\beta}$ is the deviatoric shear strain rate tensor, $\dot{\varepsilon}_{ev}^{\gamma\gamma}$ is the rates of the volumetric parts of the elastic strain tensor, $s^{\alpha\beta}$ is the deviatoric shear stress tensor, $K = E/(3(1-2\upsilon))$ is the elastic bulk modulus, $G = E/(2(1+\upsilon))$ is the shear modulus, E is Young's modulus and υ is the Poisson's ratio. The plastic multiplier rate $\dot{\lambda}$ is given by:

$$\dot{\lambda} = \frac{\bar{\eta}K\dot{\varepsilon}^{\gamma\gamma} + \dfrac{G}{\sqrt{J_2}}s^{\alpha\beta}\dot{\varepsilon}^{\alpha\beta}}{\eta\bar{\eta}K + G} \tag{A.3}$$

with the parameter η and $\bar{\eta}$ are defined in terms of the friction angle ϕ and dilatancy angle φ as

$$\eta = \frac{6\sin\phi}{\sqrt{3}(3-\sin\phi)}, \quad \bar{\eta} = \frac{6\sin\varphi}{\sqrt{3}(3-\sin\varphi)} \tag{A.4}$$

The components of the strain rate $\dot{\varepsilon}^{\alpha\beta}$ are given by:

$$\dot{\varepsilon}^{\alpha\beta} = \frac{1}{2}\left(\frac{\partial v^{\alpha}}{\partial x^{\beta}} + \frac{\partial v^{\beta}}{\partial x^{\alpha}}\right) \tag{A.5}$$

In the above equations, $F(\sigma^{\alpha\beta}, c)$ is the Drucker–Prager yield function (Deb et al 2013) and can be expressed as:

$$F(\sigma^{\alpha\beta}, c) = \sqrt{J_2(s^{\alpha\beta})} + \eta I_1(\sigma^{\alpha\beta}) - \xi c \tag{A.6}$$

where c is the ice cohesion given in Eq. (A. 9) ; $J_2(s^{\alpha\beta})$ is the second invariant of the stress tensor, and $I_1(\sigma^{\alpha\beta})$ is one third of the first invariant of the stress tensor. The parameter ξ is defined as $\xi = 6\cos\phi \Big/ \left(\sqrt{3}(3-\sin\phi)\right)$. $F(\sigma^{\alpha\beta}, c) < 0$ means that ice behaves like an elastic material while $F(\sigma^{\alpha\beta}, c) > 0$ indicates that ice undergoes the plastic deformation with $F(\sigma^{\alpha\beta}, c) = 0$ representing the yield surface.

The stress tensor estimated in Eq. (A.1) may have numerical error and lead to so-called tension cracking or unphysical stress state moving away from the yield as discussed by Bui et al. (2008). To rectify the problem, the correction must be performed as suggested

by Bui et al. (2008). That is, when $F(\sigma^{\alpha\beta},c)>0$, i.e., $\sqrt{J_2(s^{\alpha\beta})}>-\eta I_1(\sigma^{\alpha\beta})+\xi c$, the stresses are further modified as

$$\tilde{\sigma}^{\alpha\beta}=\begin{cases}\hat{\sigma}^{\alpha\beta}-\left(I_1(\hat{\sigma}^{\alpha\beta})-\dfrac{\xi c}{\eta}\right)\delta^{\alpha\beta} & \text{if } r_{sf}<0\\ \dfrac{-\eta I_1+\xi c}{\sqrt{J_2}}\hat{s}^{\alpha\beta}+I_1(\hat{\sigma}^{\alpha\beta})\delta^{\alpha\beta} & \textit{else}\end{cases} \tag{A.7}$$

where $r_{sf}=\left(-\eta I_1+\xi c\right)\big/\sqrt{J_2}$ is called as the scaling factor. In the summary, the stresses used in the ice dynamics equation are determined by

$$\sigma^{\alpha\beta}=\begin{cases}\hat{\sigma}^{\alpha\beta} & \text{if } F(\sigma^{\alpha\beta},c)\le 0\\ \tilde{\sigma}^{\alpha\beta} & \text{if } F(\sigma^{\alpha\beta},c)>0\end{cases} \tag{A.8}$$

A.2. Cohesion softening

To model the failure behaviour of ice affected by fracturing, the strain softening (Whyatt and Board, 1991) is considered by modifying the cohesion of ice as suggested by Deb and Pramanik (2013):

$$c=\max(c_0-k\bar{\varepsilon}_p,c_r) \tag{A.9}$$

where $c_0=\left(\sigma_c\sigma_t\big/\left(\sigma_c-\sigma_t\right)\right)\tan\phi$ with σ_c and σ_t being compression and tension strength which has the relationship $\phi=\sin^{-1}\left(\left(\sigma_c-\sigma_t\right)\big/\left(\sigma_c+\sigma_t\right)\right)$. The compression strength σ_c can be about third times the flexural strength σ_f. The k is the specific softening coefficient and c_r is a residual value. The k and c_r are taken as 0.1 and $c_0/50$, respectively, based on our numerical tests of the bending and compression failure progress of ice in Zhang et al. (2017). The accumulated plastic strain $\bar{\varepsilon}_p$ is estimated by $\dot{\bar{\varepsilon}}_p=\dot{\lambda}\xi$.

References

Adami, S., Hu, X. Y., Adams, N. A. (2012). A generalized wall boundary condition for smoothed particle hydrodynamics. J. Comput. Phys. 231(21), 7057-7075.

Amini, Y., Emdad, H., Farid, M. (2011). A new model to solve fluid–hypo-elastic solid interaction using the smoothed particle hydrodynamics (SPH) method. Eur. J. Mech. B-Fluid. 30(2), 184-194.

Antoci, C., Gallati, M., Sibilla, S. (2007). Numerical simulation of fluid–structure interaction by SPH. Comput. Struct. 85(11–14), 879-890.

Antuono, M., Colagrossi, A., Marrone, S., Molteni, D. (2010). Freesurface flows solved by means of SPH schemes with numerical diffusive terms. Comput. Phys. commun. 181(3), 532-549.

Bai, W., Zhang, T., Mcgovern, D. J. (2017). Response of small sea ice floes in regular waves: a comparison of numerical and experimental results. Ocean Eng. 129, 495-506.

Bouscasse, B., Colagrossi, A., Marrone, S., Antuono, M. (2013). Nonlinear water wave interaction with floating bodies in SPH. J. Fluid. Struct. 42(4), 112-129.

Bui, H., Fukagawa, R., Sako, K., Ohno, S. (2008). Lagrangian meshfree particles method (SPH) for large deformation and failure flows of geomaterial using elastic–plastic soil constitutive model. Int. J. Numer. Anal. Methods Geomech, 32(12), 1537-1570.

Baldock, T. E., Swan, C., Taylor, P.H. (1996). A laboratory study of nonlinear surface waves on water. Philos. Trans. R. Soc. London A. 354, 649–676.

Deb, D., Pramanik, R. (2013). Failure process of brittle rock using smoothed particle hydrodynamics. J. Eng. Mech. 139(11), 1551-1565.

Dumont, D., Kohout, A., Bertino, L. (2011). A wave-based model for the marginal ice zone including a floe breaking parameterization. J. Geophys. Res-Oceans. 116(C4), 1-12.

Ganesh, K. V., Islam, M. R. I., Patra, P. K., Travis, K. P. (2022). A pseudo-spring based SPH framework for studying fatigue crack propagation. Int. J. Fatigue. 162, 106986.

Gotoh, H., Shao, S. D., Memita, T. (2004). SPH-LES model for numerical investigation of wave interaction with partially immersed breakwater. Coast. Eng. J. 46(1), 39-63.

Gray, J., Monaghan, J., Swift, R. (2001). SPH elastic dynamics. Comput. Methods Appl. Mech. Eng. 190(49-50), 6641-6662.

Gutfraind, R., Savage, S. B. (1997). Smoothed particle hydrodynamics for the simulation of broken-ice fields: Mohr–Coulomb-type rheology and frictional boundary conditions. J. Comput. Phys. 134(2), 203-215.

Herman, A. (2017). Wave-induced stress and breaking of sea ice in a coupled hydrodynamic–discrete-element wave–ice model. Cryosphere Discuss. 11(6), 2711–2725.

He, J. D., Tofighi, N., Yildiz, M., Lei, J.M., Suleman, A. (2017). A coupled WC-TL SPH method for simulation of hydroelastic problems. Int. J. Comput. Fluid D. 31(3), 174-187.

He, K., Ni, B., Xu, X., Wei, H., Xue, Y. (2022). Numerical simulation on the breakup of an ice sheet induced by regular incident waves. Appl. Ocean Res. 120, 103024.

Ji, S. Y., Li, H., Shen, H. T., Wang, R., Yue, Q. (2007). A hybrid lagrangian - eulerian numerical model for sea-ice dynamics. Acta Oceanol. Sin. 26(5), 12-24.

Ji, S. Y., Shen, H. T., Wang, Z. L., Shen, H. H., Yue, Q. J. (2005). A viscoelastic-plastic constitutive model with Mohr-coulomb yielding criterion for sea ice dynamics. Acta Oceanol. Sin. 24(4), 54-65.

Jiménez, S., Duddu, R., Bassis, J. (2017). An updated-Lagrangian damage mechanics formulation for modeling the creeping flow and fracture of ice sheets. Comput. Methods Appl. Mech. Eng. 313, 406-432.

Jordaan, I. J. (2001). Mechanics of ice–structure interaction. Eng. Fract. Mech. 68 (17),1923–1960.

Joshi, S., Franc, J. P., Ghigliotti, G., Fivel, M. (2019). SPH modelling of a cavitation bubble collapse near an elasto-visco-plastic material. J. Mech. Phys. Solids. 125, 420-439.

Khayyer, A., Gotoh, H., Shao, S. D. (2008). Corrected incompressible SPH method for accurate water surface tracking in breaking waves. Coastal Eng. 55(3), 236-250.

Khayyer, A., Shimizu, Y., Gotoh, H., Nagashima, K. (2021). A coupled incompressible SPH-Hamiltonian SPH solver for hydroelastic FSI corresponding to composite structures. Appl. Math. Model. 94(1).

Khayyer, A., Shimizu, Y., Gotoh, H., Hattori, S. (2022). A 3D SPH-based entirely Lagrangian meshfree hydroelastic FSI solver for anisotropic composite structures. Appl. Math. Model. 112, 560-613.

Kohout, A. L., Williams, M. J. M., Toyota, T., Lieser, J., Hutchings, J. (2016). In situ observations of wave-induced sea ice breakup. Deep-Sea Res. Pt. II. 131, 22-27.

Libersky LD, Petschek AG. (1991). Smoothed particle hydrodynamics with strength of materials. In Proceedings of the Next Free Lagrange Conference, Trease H, Friits J, Crowley W (eds). Springer: New York, 395, 248-257.

Luo, M., Khayyer, A., Lin, P. Z. (2021). Particle methods in ocean and coastal engineering. Appl. Ocean Res. 114, 102734.

Ma, Q. W. (2007). Numerical generation of freak waves using MLPG_R and QALE-FEM methods. Comput. Model. Eng. Sci. 18(3), 223-234.

Ma, Q.W. (2008). A new meshless interpolation scheme for MLPG_R method. CMES-Comp Model. Eng. 23(2), 75-89.

Ma, Q. W., Zhou, J. (2009). MLPG_R method for numerical simulation of 2D breaking waves. Comput. Model. Eng. Sci. 43, 277-304.

Macia, F., Antuono, M., González, L. M., Colagrossi, A. (2011). Theoretical analysis of the no-slip boundary condition enforcement in SPH methods. Prog. Theor. Phys. 125(6), 1091-1121.

Meylan, M.H., Bennetts, L.G., Cavaliere, C., Alberello, A., Toffoli, A. (2015). Experimental and theoretical models of wave-induced flexure of a sea ice floe. Phys. Fluids. 27(4), L24610.

Mokus, N. G. A., Montiel, F. (2021). Wave-triggered breakup in the marginal ice zone generates lognormal floe size distributions. The Cryosphere Discussions, 1-33.

Monaghan, J. J., Gingold R. A. (1983). Shock simulation by the particle method SPH. J. Comput. Phys. 52:374–89.

Monaghan, J. J. (1992). Smoothed particle hydrodynamics. Annu. Rev. Astron. Astrophys, 30, 543-574.

Monaghan, J. J. (2000). SPH without a tensile instability. J. Comput. Phys. 159(2), 290-311.

Montiel, F., Squire, V. A. (2017). Modelling wave-induced sea ice break-up in the marginal ice zone. P. Roy. Soc. A-Math. Phy. 473(2206).

Morris, J., Fox, P., Zhu, Y. (1997). Modeling low Reynolds number incompressible flows using SPH. J. Comput. Phys. 136(1), 214–226.

Mu, D., Qu, H., Zeng, Y., Tang, A. (2023). An improved SPH method for simulating crack propagation and coalescence in rocks with pre-existing cracks. Eng. Fract. Mech. 282, 109148.

Oger, L., Savage, S. B. (1999). Smoothed particle hydrodynamics for cohesive grains. Comput Methods Appl Mech Eng. 180(1-2), 169-183.

Randles, P, Libersky, L. (1996). Smoothed particle hydrodynamics: some recent improvements and applications. Comput. Methods Appl. Mech. Eng. 139(1), 375-408.

Ren, B., He, M., Dong, P., Wen, H. (2015). Nonlinear simulations of wave-induced motions of a freely floating body using wcsph method. Appl. Ocean Res. 50, 1-12.

Ren, D., Park, J. C. (2023). Particle-based numerical simulation of continuous ice-breaking process by an icebreaker. Ocean Eng. 270, 113478.

Ren, H., Zhang, C., Zhao, X. (2021). Numerical simulations on the fracture of a sea ice floe induced by waves. Appl. Ocean Res. 108, 102527.

Ren, Y., Khayyer, A., Lin, P., Hu, X. (2023). Numerical modeling of sloshing flow interaction with an elastic baffle using SPHinXsys. Ocean Eng. 267, 113110.

Sanderson, T. (1988). Ice Mechanics-Risks to Offshore Structures. Graham & Trotman, London, pp. 1–253.

Schulson, E.M. (2001). Brittle failure of ice. Eng. Fract. Mech. 68 (17), 1839–1887.

Shi, C., Hu, Z., Ringsberg, J., Luo, Y. (2017). Validation of a temperature-gradient-dependent elastic-plastic material model of ice with finite element simulations. Cold Reg. Sci. Technol. 133, 15-25.

Swegle, J., Hicks, D., Attaway, S. (1995). Smoothed particle hydrodynamics stability analysis. J. Comput. Phys. 116(1), 123-134.

Shao, S. D., Lo, E. Y. M. (2003). Incompressible SPH method for simulating newtonian and non-newtonian flows with a free surface. Adv. Water Resour. 26(7), 787-800.

Shao, S. D. (2010). Incompressible SPH flow model for wave interactions with porous media. Coast. Eng. 57(3), 304-316.

Shen, H. H., Ackley, S. F. (1991). A one-dimensional model for wave-induced ice-floe collisions. Ann. Glaciol. 15, 87-95.

Shen, H. T., Su, J., Liu, L. (2000). SPH simulation of river ice dynamics. J. Comput. Phys. 165(2), 752-770.

Silling, S.A., Askari, E. (2005). A meshfree method based on the peridynamic model of solid mechanics. Comput. Struct. 83 (17), 1526–1535.

Squire, V. A. (1981), Numerical simulation of ice floes in waves, Tech. Rep. 81-1, 57 pp., Scott Polar Res. Inst., Cambridge, U. K.

Squire, V. A. (2007). Of ocean waves and sea-ice revisited. Cold Reg. Sci. Technol. 49(2), 110-133.

Squire, V. A. (2011). Past, present and impendent hydroelastic challenges in the polar and subpolar seas. Phil. Trans. R. Soc. A. 369(1947), 2813-2831.

Steele, M. (1992). Sea ice melting and floe geometry in a simple ice-ocean model. J. Geophys. Res-oceans. 97(C11), 17729-17738.

Takeda, H., Miyama, S. M., Sekiya, M. (1994). Numerical simulation of viscous flow by smoothed particle hydrodynamics. Prog. Theor. Phys. 92(5), 939-960.

Wang, R., Shen, H. H. (2011). A continuum model for the linear wave propagation in ice-covered oceans: an approximate solution. Ocean Model. 38, 244–250.

Wang, Y., Tran, H. T., Nguyen, G. D., Ranjith, P. G., Bui, H. H. (2020). Simulation of mixed-mode fracture using SPH particles with an embedded fracture process zone. Int. J. Numer. Anal. Met. 44(10), 1417-1445.

Wang, Y. X., Li, C. H., Li, G.W., Shen, Z. W. (2000). Experimental investigation on breakup of ice floe on waves. China, Ocean Eng. 14(4), 511-516.

Westphalen, J., Greaves, D. M., Williams, C. J. K., Hunt-Raby, A. C., Zang, J. (2012). Focused waves and wave-structure interaction in a numerical wave tank. Ocean Eng. 45(5), 9-21.

Whyatt, J. K., Board M. P. Numerical exploration of shear-fracture-related rock bursts using a strain-softening constitutive law. US Department of the Interior, Bureau of Mines; 1991.

Williams, T. D., Bennetts, L. G., Dumont, D., Squire, V. A., Bertino, L. (2013a). Wave-ice interactions in the marginal ice zone. Part 1: Theoretical foundations. Ocean Model. 71, 81–91.

Williams, T. D., Bennetts, L. G., Dumont, D., Squire, V. A., Bertino, L. (2013b). Wave-ice interactions in the marginal ice zone. Part 2: Numerical implementation and sensitivity studies along 1d transects of the ocean surface. Ocean Model. 71, 92–101.

Xu, Z., Tartakovsky, A. M., Pan, W. (2012). Discrete-element model for the interaction between ocean waves and sea ice. Phys. Re. E. 85(2), 016703.

Yiew, L. J. (2017) Modelling the Wave-Induced Collisions of Ice Floes. PhD thesis, University of Adelaide.

You, Y., Khayyer, A., Zheng, X., Gotoh, H., Ma, Q. W. (2021). Enhancement of δ-SPH for ocean engineering applications through incorporation of a background mesh scheme. Appl. Ocean Res. 102508.

Zhan, L., Peng, C., Zhang, B., Wu, W. (2019). A stabilized TL-WC SPH approach with GPU acceleration for three-dimensional fluid–structure interaction. J. Fluid Struct. 86, 329-353.

Zhang, C., Zhao, X. (2021). Theoretical model for predicting the break-up of ice covers due to wave-ice interaction. Appl. Ocean Res. 112, 102614.

Zhang, N. B., Zheng, X., Ma, Q. W. (2017). Updated smoothed particle hydrodynamics for simulating bending and compression failure progress of ice. Water. 9(11), 882.

Zhang, N. B., Zheng, X., Ma, Q. W. et al. (2018). A hybrid stabilization technique for simulating water wave–structure interaction by incompressible smoothed particle hydrodynamics (ISPH) method. J. Hydro-environ. Res. 18:77-94.

Zhang, N. B., Zheng, X., Ma, Q. W. (2019). Study on wave-induced kinematic responses and flexures of ice floe by smoothed particle hydrodynamics. Comput. Fluid. 189, 46-59.

Zhang, N. B., Zheng, X., Ma, Q. W., Hu, Z. H. (2019). A numerical study on ice failure process and ice-ship interactions by Smoothed Particle Hydrodynamics. Int. J. Nav. Arch. Ocean. 11(2), 796-808.

Zheng, X., Ma, Q. W., Duan, W. Y. (2014). Incompressible SPH method based on Rankine source solution for violent water wave simulation. J. Comput. Phys. 276, 291-314.